Heat capacity double transitions in time-reversal symmetry broken superconductors

Henrik S. Røising ®,[1,*] Glenn Wagner ®,[2] Mercè Roig ®,[1] Astrid T. Rømer,[1,3] and Brian M. Andersen ®[1]

[1]*Niels Bohr Institute, University of Copenhagen, DK-2200 Copenhagen, Denmark*
[2]*Department of Physics, University of Zurich, Winterthurerstrasse 190, 8057 Zurich, Switzerland*
[3]*Danish Fundamental Metrology, Kogle Allé 5, 2970 Hørsholm, Denmark*

Standard superconductors display a ubiquitous discontinuous jump in the electronic specific heat at the critical superconducting transition temperature. In a growing class of unconventional superconductors, however, a second order parameter component may get stabilized and produce a second heat capacity jump at a lower temperature, typically associated with the spontaneous breaking of time-reversal symmetry. The splitting of the two specific heat discontinuities can be controlled by external perturbations such as chemical substitution, hydrostatic pressure, or uniaxial strain. We develop a theoretical quantitative multiband framework to determine the ratio of the heat capacity jumps, given the band structure and the order parameter momentum structure. We discuss the conditions of the gap profile which determine the amplitude of the second jump. We apply our formalism to the case of Sr_2RuO_4, and using the gap functions from a microscopic random phase approximation calculation, we show that recently proposed accidentally degenerate order parameters may exhibit a strongly suppressed second heat capacity jump. We discuss the origin of this result and consider also the role of spatial inhomogeneity on the specific heat. Our results provide a possible explanation of why a second heat capacity jump has so far evaded experimental detection in Sr_2RuO_4.

I. INTRODUCTION

A growing number of superconductors realize multicomponent condensates, some with clear evidence for spontaneous time-reversal symmetry breaking (TRSB) below the critical superconducting transition temperature T_c [1]. Such states of matter exhibit persistent supercurrents at material edges, dislocations, or around nonmagnetic defect sites [2,3]. The term "multicomponent" refers to real or complex superpositions of two allowed symmetry-distinct pairing symmetries. An important bulk thermodynamic probe which can determine the associated phase transitions is specific heat measurements. Possible multicomponent superconductors of current interest include several uranium-based materials UPt_3 [4,5], UTe_2 [6,7], URu_2Si_2 [8,9], but also compounds like Sr_2RuO_4 [10,11], $Ba_{1-x}K_xFe_2As_2$ [12,13], $LaNiC_2$ [14], and $PrOs_4Sb_{12}$ [15,16]. Here, particularly UPt_3 is known to exhibit a clear double transition possibly into an exotic low-temperature spin-triplet $f + if$ superconducting state [5]. At present, the nature of superconductivity in UTe_2 and Sr_2RuO_4 is controversial and of high interest to the community. In this respect, the recent discovery of a large Knight shift suppression [17,18] in the superconducting state of Sr_2RuO_4 has ignited tremendous renewed interest in the exploration of the superconducting state of this material. Cooper pairing in Sr_2RuO_4 is not of predominant spin-triplet character, but rather of the spin-singlet form. The stakes are significant, not just because of a desire to explain superconductivity in this

particular compound, but also because it challenges our ability to experimentally determine, and theoretically describe, unconventional superconductivity arising from many-body instabilities in Fermi liquids. At present, it is unclear whether the standard framework for unconventional superconductivity in terms of repulsive short-range Coulomb interactions properly captures the pairing structure of Sr_2RuO_4. The theoretical description is complicated by a large spin-orbit coupling and a multiband (multiorbital) Fermi surface, which likely supports several near-degenerate symmetry-distinct superconducting phases [19–23].

The current status of superconductivity in Sr_2RuO_4 can be condensed into the following open question: what nodal spin-singlet time-reversal symmetry breaking superconducting multicomponent order parameter, whose product transforms as B_{2g}, is realized below T_c? As mentioned above, nuclear magnetic resonance dictates a condensate of primarily spin-singlet nature, implying even-parity Cooper pairs. Spectroscopic probes [24,25], specific heat [26,27], and thermal conductivity measurements [28] are consistent with nodal quasiparticle excitations. Optical Kerr rotation measurements [29] and muon spin relaxation (μSR) [30] find evidence for TRSB below T_c, and ultrasound experiments also point to multicomponent condensates [31,32]. Specifically, the presence of a discontinuity in the shear elastic modulus c_{66} (the B_{2g} channel) at T_c seems only consistent with situations where the product of the two involved order parameters transforms as the B_{2g} irreducible representation (irrep) of the point group D_{4h} relevant for Sr_2RuO_4 [31,32]. Thus at face value these constraints allow only $d_{xz} + id_{yz}$ [33,34], $s' + id_{xy}$ [23,35], and $d_{x^2-y^2} + ig_{xy(x^2-y^2)}$ [36,37] orders. (We denote by s' an

*henrik.roising@nbi.ku.dk

order parameter with a nodal spectrum and A_{1g} symmetry. We note that nodal quasiparticles for the $s' + id_{xy}$ scenario require matching of accidental nodes for the two components.) Of these candidates the former is attractive due to its inherent 2D irrep character, but appears unlikely from its nodal properties and 3D nature [20,38]. In addition, $d_{xz} + id_{yz}$ implies a coupling to the $(c_{11} - c_{12})/2$ (B_{1g}) shear channel, which has not been observed. On the other hand, the latter two candidates currently appear consistent with all the recent developments summarized above, but require fortuitous degeneracy between s' and d_{xy}, or $d_{x^2-y^2}$ and $g_{xy(x^2-y^2)}$ pairing symmetries.

For all these mentioned multicomponent pairing candidates, however, there is an important "fly in the ointment" that needs to be addressed. Specific heat measurements under uniaxial pressure up to around 0.6 GPa detect only a single phase transition even as the leading T_c rises from 1.5 to 3.5 K [27]. This points to a superconducting phase consisting of a single order parameter. Nevertheless, pursuing the multicomponent candidates further, the naive expectation of such a symmetry-breaking perturbation would be a split transition with two associated distinguishable peaks in the specific heat versus temperature. Indeed this particular issue has given rise to alternative scenarios for Sr_2RuO_4 based on inhomogeneous phases with secondary order parameter components stabilized only near edge dislocations of the crystal structure [37]. Alternatively, the second transition may simply be very weak and so far indiscernable experimentally. According to Ref. [27], this requires that the second transition be less than ∼5% of the primary phase transition discontinuity. Previous theoretical investigations of the size of the second specific heat jump were reported in Ref. [39] where a microscopically derived Ginzburg-Landau approach was taken to numerically explore the specific heat of mainly a $d_{x^2-y^2} + ig_{xy(x^2-y^2)}$ solution in the unstrained case.

Here, we perform a general theoretical investigation of the specific heat transition of double-component superconducting phase transitions, and identify the key conditions determining the ratio of the amplitudes of the specific heat jumps at the two transition temperatures. This study is of relevance to all TRSB two-component superconducting phase transitions. In addition, we compute the specific heat explicitly from recent microscopically obtained $s' + id_{xy}$ and $d_{x^2-y^2} + ig_{xy(x^2-y^2)}$ superconducting orders specific to Sr_2RuO_4, and consider the effects of uniaxial strain and spatial inhomogeneity. We discuss the results in light of the recent specific heat measurements on Sr_2RuO_4, and conclude that the fortuitously degenerate superconducting candidate orders obtained from realistic material-specific models are consistent with currently available specific heat data.

The paper is organized as follows. In Sec. II we derive the ratio of the heat capacity jumps for a general two-component order parameter. The result is explored within a microscopic Ginzburg-Landau framework, and with a numerical demonstration in a simple one-band model. In Sec. III we apply our formalism to the case of Sr_2RuO_4 by calculating the heat capacity for two recently proposed order parameter candidates as a function of uniaxial in-plane strain. In Sec. IV we discuss a series of other putative time-reversal symmetry broken superconductors with possible double transitions in light of our results at the qualitative level. The paper is
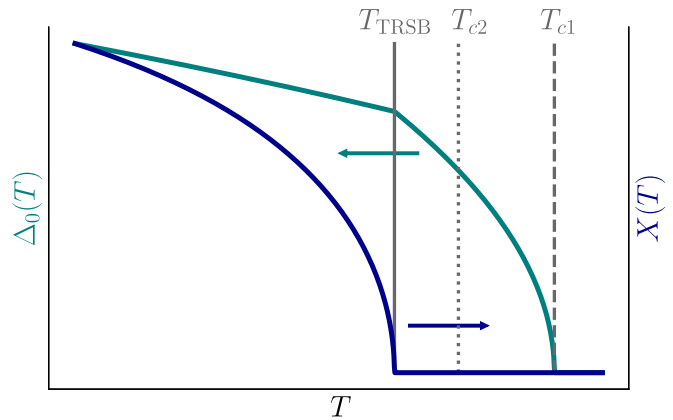

FIG. 1. Sketch of the order parameter temperature dependence, where $\Delta(T, \boldsymbol{p}) = \Delta_0(T)[f_a(\boldsymbol{p}) + iX(T)f_b(\boldsymbol{p})]$. When the two components have critical temperatures $T_c := T_{c1}$ and T_{c2}, repulsion leads to the onset of the second component at $T_{TRSB} < T_{c2}$, for which time-reversal symmetry is broken (blue line). Due to repulsion $\Delta_0(T)$ (green line) becomes nonanalytic at T_{TRSB}. The nonanalyticity leads to a reduction of the second heat capacity jump.

concluded in Sec. V. In Appendix A we provide details of the derivation of the heat capacity in multiband superconductors. Appendix B includes a self-contained derivation of the microscopic Ginzburg-Landau approach. In Appendix C we list the three-band tight-binding model of Sr_2RuO_4 and its strain parametrization, and in Appendix D we provide supplementary heat capacity plots for Sr_2RuO_4.

II. HEAT CAPACITY OF MULTICOMPONENT SUPERCONDUCTORS

We consider a two-component order parameter with a general temperature dependence, as parametrized by the two functions $\Delta_0(T)$ and $X(T)$:

$$\Delta(T, \boldsymbol{p}) = \Delta_0(T)[f_a(\boldsymbol{p}) + iX(T)f_b(\boldsymbol{p})]. \quad (1)$$

Here, a and b are symmetry labels denoting two different one-dimensional irreducible representations (irreps) of the appropriate point group. The order parameter is in general multiband; a band index has been left implicit in the above ansatz. The form factors are normalized as $\max_{\boldsymbol{p} \in FS} |f_{a/b}(\boldsymbol{p})| = 1$.

In the current scenario where the two components of the condensate belong to different irreps, the temperatures at which $\Delta_0(T)$ and $X(T)$ onset, which we denote by T_c and T_{TRSB}, respectively, are generally different. Generically, recondensation at T_{TRSB} makes $\Delta_0(T)$ nonanalytic at this temperature, which has important consequences for the second specific heat jump that we address in detail in the following. Sketches of the temperature dependencies of Δ_0 and X are shown in Fig. 1.

A. The heat capacity discontinuities

The heat capacity of a superconductor, $C(T) = T \partial S / \partial T$, is derived from the entropy of the free Fermi gas [40] (see

also Appendix A for a detailed derivation)

$$S = -2 \sum_{\mu,\boldsymbol{k}} [n_F[E_\mu(\boldsymbol{k})] \ln n_F[E_\mu(\boldsymbol{k})]$$
$$+ (1 - n_F[E_\mu(\boldsymbol{k})]) \ln(1 - n_F[E_\mu(\boldsymbol{k})])], \quad (2)$$

where $n_F(E)$ denotes the Fermi function and $E_\mu(\boldsymbol{k})$ is the quasiparticle excitation energy of band μ at momentum $\boldsymbol{k}$. As the electrons condense into Cooper pairs, both at the primary (T_c) and the secondary (T_{TRSB}) transitions, there is an associated reduction of entropy that results in a discontinuous jump in the heat capacity. We define the heat capacity jumps as the change in value across the respective transitions, $\Delta C_{\mathrm{SC}}/T_c := [\lim_{T \to T_c^-} C(T) - \lim_{T \to T_c^+} C(T)]/T_c$ and $\Delta C_{\mathrm{TRSB}}/T_{\mathrm{TRSB}} := [\lim_{T \to T_{\mathrm{TRSB}}^-} C(T) - \lim_{T \to T_{\mathrm{TRSB}}^+} C(T)]/T_{\mathrm{TRSB}}$. It is a straightforward task to calculate the ratio of the two jumps in the thermodynamic limit, which we denote by η, starting from Eq. (2) and using the general order parameter ansatz of Eq. (1). We provide the details of this calculation in Appendix A and summarize the main result here. When η is expressed as a Fermi surface average, the final result reads

$$\eta = \frac{\Delta C_{\mathrm{TRSB}}/T_{\mathrm{TRSB}}}{\Delta C_{\mathrm{SC}}/T_c}$$
$$= \frac{T_c}{T_{\mathrm{TRSB}}} \left[A \frac{\langle |f_a(\boldsymbol{p})|^2 \mathcal{I}[z(\boldsymbol{p})] \rangle_{\mathrm{FS}}}{\langle |f_a(\boldsymbol{p})|^2 \rangle_{\mathrm{FS}}} + B \frac{\langle |f_b(\boldsymbol{p})|^2 \mathcal{I}[z(\boldsymbol{p})] \rangle_{\mathrm{FS}}}{\langle |f_a(\boldsymbol{p})|^2 \rangle_{\mathrm{FS}}} \right]. \quad (3)$$

This result comes about as two terms are picked up in the evaluation of $\Delta C_{\mathrm{TRSB}}/T_{\mathrm{TRSB}}$ since generally the temperature dependencies of both order parameter components, $\Delta_0^2(T)$ and $\Delta_0^2(T)X^2(T)$, are nonanalytic at T_{TRSB}, as caused by terms in the free energy that couple the two components. Formally, the nonanalyticity is expressed via

$$A = Q(\Delta_0, T_{\mathrm{TRSB}})/Q(\Delta_0, T_c), \quad (4)$$

$$B = Q(\Delta_0 X, T_{\mathrm{TRSB}})/Q(\Delta_0, T_c), \quad (5)$$

$$Q(g, T_0) := \lim_{T \to T_0^-} \frac{\partial g^2(T)}{\partial T} - \lim_{T \to T_0^+} \frac{\partial g^2(T)}{\partial T}. \quad (6)$$

Finally, in Eq. (3) we introduced the dimensionless integral $\mathcal{I}(z) := \int_0^\infty du \, \cosh^{-2}(\sqrt{u^2 + z^2})$ with $z(\boldsymbol{p}) = \frac{\Delta_0(T_{\mathrm{TRSB}})}{2T_{\mathrm{TRSB}}} f_a(\boldsymbol{p})$, and the Fermi surface averages are evaluated as $\langle f \rangle_{\mathrm{FS}} := \sum_\mu \int_{S_\mu} \frac{d\boldsymbol{k}}{(2\pi)^d} \frac{f}{v_\mu(\boldsymbol{k})}$, with $v_\mu(\boldsymbol{k}) = |\nabla \xi_\mu(\boldsymbol{k})|$ being the Fermi velocity of band μ.

In the particular case of $\Delta_0(T)$ being analytic at T_{TRSB}, we see that $A = 0$. In the BCS-like case of $\Delta_0(T) = \Delta_{0a}(1 - T/T_c)^{1/2}$ and $X(T) = \Delta_{0b}/\Delta_{0a}[(1 - T/T_{\mathrm{TRSB}})/(1 - T/T_c)]^{1/2}$ we recover the result of Ref. [36], i.e.,

$$\eta_0 = \left(\frac{T_c}{T_{\mathrm{TRSB}}} \right)^2 \left(\frac{\Delta_{0b}}{\Delta_{0a}} \right)^2 \frac{\langle |f_b(\boldsymbol{p})|^2 \mathcal{I}[z(\boldsymbol{p})] \rangle_{\mathrm{FS}}}{\langle |f_a(\boldsymbol{p})|^2 \rangle_{\mathrm{FS}}}. \quad (7)$$

We stress that when the two order parameter components repel, the resulting nonanalyticity of $\Delta_0(T)$ suppresses the second heat capacity jump, with the conditions for an observable second transition being quantitatively dictated by Eq. (3).

B. Ginzburg-Landau theory

To shed light on the heat capacity jump ratio in Eq. (3), which involves the temperature dependence of the two order parameter components, and to facilitate a calculation of the coefficients A and B, we turn to a microscopic Ginzburg-Landau theory building on seminal work by Gor'kov [41]. For a multicomponent order parameter we derive the general quartic-order free energy in the superconducting phase in Appendix B, with further details given in Ref. [39]. In the two-component case of Eq. (1), when explicitly including band indices μ, the free energy takes the form

$$\Delta F = \Delta_0^2(T)[\alpha_a(T, T_{c1}) + \alpha_b(T, T_{c2})X^2(T)]$$
$$+ \Delta_0^4(T)[\beta_a + 2\beta_{ab}X^2(T) + \beta_b X^4(T)], \quad (8)$$

where

$$\alpha_j(T, T_{cj}) = -V \sum_\mu \int \frac{d\boldsymbol{p}}{(2\pi)^d} \left(\frac{\tanh[\xi_\mu(\boldsymbol{p})/(2T)]}{2\xi_\mu(\boldsymbol{p})} \right.$$
$$\left. - \frac{\tanh[\xi_\mu(\boldsymbol{p})/(2T_{cj})]}{2\xi_\mu(\boldsymbol{p})} \right) f_{j\mu}^2(\boldsymbol{p}), \quad (9)$$

$$\beta_j = \sum_\mu \frac{V}{2T_{c1}^3} \int \frac{d\boldsymbol{p}}{(2\pi)^d} h(\xi_\mu(\boldsymbol{p})/T_{c1}) f_{j\mu}^4(\boldsymbol{p}), \quad (10)$$

$$\beta_{ab} = \sum_\mu \frac{V}{2T_{c1}^3} \int \frac{d\boldsymbol{p}}{(2\pi)^d} h(\xi_\mu(\boldsymbol{p})/T_{c1}) f_{a\mu}^2(\boldsymbol{p}) f_{b\mu}^2(\boldsymbol{p}), \quad (11)$$

with V being the reciprocal space volume, $j = a, b$, and $h(x) \geqslant 0$ is sharply peaked around $x = 0$ for low temperatures and is given in Eq. (B12). Above, we asserted that f_a condenses at T_{c1} and f_b at T_{c2}.

The free energy is minimized over $\Delta_0(T)$ and $X(T)$, and in Appendix B 2 we show that this results directly in $T_c = T_{c1}$ and $T_{\mathrm{TRSB}} = T_{\mathrm{TRSB}}(T_{c1}, T_{c2}) \leqslant T_{c2}$ (equality when $\beta_{ab} = 0$). Since the temperature dependence of the quartic order is weak and not a leading-order effect, we evaluate the β's at $T = T_c$. When further using $\alpha_j(T, T_{cj}) = \alpha_j^0(T/T_{cj} - 1)$ with $\alpha_j^0 \geqslant 0$, which holds close to the respective transition temperatures, we find that the Ginzburg-Landau solution yields

$$A = -\frac{\beta_{ab}}{\beta_a \beta_b - \beta_{ab}^2} \left[\beta_{ab} + \frac{\alpha_b^0}{\alpha_a^0} \frac{T_c}{T_{\mathrm{TRSB}}} \beta_a \right], \quad (12)$$

$$B = \frac{\beta_a}{\beta_a \beta_b - \beta_{ab}^2} \left[\frac{\alpha_b^0}{\alpha_a^0} \frac{T_c}{T_{\mathrm{TRSB}}} \beta_a - \beta_{ab} \right], \quad (13)$$

for the coefficients in Eq. (3). Owing to Hölder's inequality it follows that $\beta_a \beta_b - \beta_{ab}^2 \geqslant 0$. Moreover, since $\beta_b, \beta_a \geqslant 0$, we conclude that $A \leqslant 0$ and that B in principle can take both signs but is only physically relevant in the positive-semidefinite regime to yield an overall positive η.

It is worth noting that the free energy of Eq. (8), derived in the case where the two order parameter components belong to different one-dimensional irreps of D_4, still holds under uniaxial in-plane strain where the crystal symmetries are reduced, $D_4 \to D_2$ (note that D_2 only permits one-dimensional irreps); cf. Ref. [42]. Strain modifies both the band structure ξ_μ and the form factors $f_{a\mu}(\boldsymbol{p})$, but as long as the form factors are

labeled appropriately by the irreps of the symmetry-reduced point group D_2, the coefficients in Eqs. (9)–(11) still apply.

C. Parameters controlling the magnitude of the second jump

The expression of Eq. (3), along with the Ginzburg-Landau result of Eqs. (12) and (13), reveals the key knobs that dictate the size of the second heat capacity jump.

First, η is generally highly sensitive to the order of which the order parameter components onset. Intuitively, the more of the Fermi surface that is gapped out by the primary component (at T_c), or correspondingly the fewer the quasiparticles left to be gapped out by the secondary component (at T_{TRSB}), the smaller the second jump. This can be inferred directly from Eq. (3) by the fact that $\langle |f_a(\boldsymbol{p})|^2 \rangle_{FS}$ appears in the denominators, so the order of the components is decisive for the size of η.

Second, η is suppressed in cases where the two components share momentum structure over the Fermi surface. This can be seen from the behavior of the dimensionless integral appearing in Eq. (3), $\mathcal{I}(z) \approx \exp[-7\zeta(3)z^2/\pi^2]$ [accurate to $O(z^2)$]. The second and dominant term in Eq. (3) is therefore approximately proportional to $\langle |f_b(\boldsymbol{p})|^2 \exp[-c|f_a(\boldsymbol{p})|^2] \rangle_{FS}$, where c is a positive constant. This expression will be small if, for a given momentum on the Fermi surface, $|f_a(\boldsymbol{k})|$ is maximal (minimal) where $|f_b(\boldsymbol{k})|$ is maximal (minimal). Consequentially, if the two components have a similar momentum structure over the Fermi surface, the second heat capacity jump is suppressed. In cases where the Fermi velocity is anisotropic, the regions with minimal velocity (particularly in the vicinity of van Hove points) will dominate the Fermi surface average and dictate where a matching momentum structure is decisive to get a suppressed second jump. We note that this criterion of a matching momentum structure is generally not limited to nodal regions, which is commonly accepted, but applies in principle to the entire Fermi surface.

Third, but indirectly related to the second point, increasing the repulsion between the components reduces the second jump. The repulsion is controlled by β_{ab}, which A [in Eq. (12)] is directly proportional to. This is related to the second point because β_{ab} is maximized when the components $f_a(\boldsymbol{p})$ and $f_b(\boldsymbol{p})$ share momentum structure. Technically, the closer one is to saturating Hölder's inequality $\beta_{ab}^2 \leqslant \beta_a \beta_b$, the smaller the second jump.

Since a and b label different one-dimensional irreps both symmetry-breaking and symmetry-preserving perturbations (with respect to the point group), commonly labeled ϵ, will *a priori* cause a splitting of T_c and T_{TRSB} since $\partial T_{c1}/\partial \epsilon \neq \partial T_{c2}/\partial \epsilon$ generally, and the ratio T_c/T_{TRSB} largely controls η. In the limit $\frac{T_c}{T_{TRSB}} \gg \frac{\alpha_a^0}{\alpha_b^0} \frac{\beta_{ab}}{\beta_a}$ Eqs. (12) and (13) tell us that $\eta \propto (T_c/T_{TRSB})^2$.

Experimentally, natural symmetry-preserving perturbations to consider include, e.g., disorder, impurity doping [43], and hydrostatic pressure. In the case of Sr_2RuO_4, La substitution of Sr, taking the effective role of added disorder [44], and moderate hydrostatic pressure were applied, both resulting in no detectable temperature splitting [45]. In this case, it would also be of interest to see the result of Co and Mn substitution of Ru since this has been shown to enhance

ferromagnetic and antiferromagnetic fluctuations, respectively [46,47]. Symmetry-breaking perturbations of experimental relevance include strain, which fundamentally decomposes into five types in the case of D_4: two compressional modes preserve the crystal symmetries, and three shear modes reduce the crystal symmetries [31]. In Sr_2RuO_4 the (strikingly different) effects of both symmetry-breaking (100) strain [48] and symmetry-preserving (001) strain [49] have been studied.

D. Demonstration: Circular Fermi surface

In this section we demonstrate the basic principles stated in Sec. II C for controlling the size of the second specific heat jump by calculating the heat capacity discontinuity from Eq. (3) in the simplest case of a circular Fermi surface with $\Delta_0(T) = \Delta_{0a}(1 - T/T_c)^{1/2}$ and $X(T) = \Delta_{0b}/\Delta_{0a}[(1 - T/T_{TRSB})/(1 - T/T_c)]^{1/2}$. The circular Fermi surface emerges, for example, on the square lattice with nearest-neighbor hopping, $\xi(\boldsymbol{k}) = -2t(\cos k_x + \cos k_y) - \mu$, in the low-filling limit $\mu \approx -4t$: $k_x^2 + k_y^2 = k_F^2$, with $k_F = \sqrt{4 + \mu/t}$ [50]. In this case the Fermi velocity, Fermi surface area, and density of states simplify to $v_F = 2tk_F$, $|S| = 2\pi k_F$, and $\rho_0 = k_F/(4\pi t)$, respectively. The Fermi surface averages reduce to $\langle f \rangle_{FS} = \frac{1}{2\pi k_F} \int_0^{2\pi} d\theta \, f(\theta)$, where θ is the polar angle.

We consider a perturbation ϵ that causes a splitting of T_c and T_{TRSB}. In the unperturbed case we assume that the two temperatures $T_c^{\epsilon=0} \approx T_{TRSB}^{\epsilon=0}$ such that the splitting can be meaningfully expanded in the small quantity $y := 1 - T_{TRSB}^\epsilon/T_c^\epsilon$. We further assume, as is standard, that the magnitudes of the order parameter components scale with the respective temperatures, i.e., $\Delta_{0a}^\epsilon = \Delta_{0a}^{\epsilon=0} T_c^\epsilon/T_c^{\epsilon=0}$ and $\Delta_{0b}^\epsilon = \Delta_{0b}^{\epsilon=0} T_{TRSB}^\epsilon/T_{TRSB}^{\epsilon=0}$. Consequentially, we find that η to leading order in y is given by

$$\eta = \left(\frac{\Delta_{0b}^{\epsilon=0}}{\Delta_{0a}^{\epsilon=0}} \right)^2 \frac{\langle |f_b(\theta)|^2 \rangle_{FS}}{\langle |f_a(\theta)|^2 \rangle_{FS}} \left[1 - y \frac{7\zeta(3)}{\pi^2} \left(\frac{\Delta_{0a}^{\epsilon=0}}{2T_c^{\epsilon=0}} \right)^2 \right.$$
$$\left. \times \frac{\langle |f_a(\theta)|^2 |f_b(\theta)|^2 \rangle_{FS}}{\langle |f_b(\theta)|^2 \rangle_{FS}} + O(y^2) \right]. \tag{14}$$

To obtain the above expression we made use of the small argument expansion of the dimensionless integral, $\mathcal{I}(z)$; see Appendix A 2. Notably, we see that the $O(y)$ correction is negative semidefinite under the above conditions, so the leading effect of, e.g., uniaxial in-plane strain ($\epsilon = \varepsilon_{xx}$) is a reduction of the second heat capacity jump.

From here it is a simple task to calculate the ratios of Fermi surface averages appearing in Eq. (14) for, e.g., any harmonic of the one-dimensional D_4 irreps, i.e., $f_{A_1}^{(n)}(\theta) = \cos(4n\theta)$, $f_{A_2}^{(n)}(\theta) = \sin([4n + 4]\theta)$, $f_{B_1}^{(n)}(\theta) = \cos([4n + 2]\theta)$, $f_{B_2}^{(n)}(\theta) = \sin([4n + 2]\theta)$. Focusing on the fundamental harmonic $n = 0$ we see that $\langle |f_a^{(0)}(\theta)|^2 \rangle_{FS} = \frac{1}{k_F}, \frac{1}{2k_F}$ for $a = A_1$, $\{A_2, B_1, B_2\}$, respectively. Thus, the strongest suppression of the second jump at $y = 0$ occurs for $a = A_1$ (fully gapped s wave) and $b \in \{A_2, B_1, B_2\}$ ($g_{xy(x^2-y^2)}$, $d_{x^2-y^2}$, and d_{xy}, respectively). The largest $O(y)$ corrections

occur when the nodes are maximally shifted, e.g., for $a = B_1$ and $b = B_2$. The $O(y)$ correction is minimal when the nodes are perfectly matching, e.g., for $a = b = B_1$.

E. Demonstration: Numerical evaluation

To further illustrate the points made in the preceding sections, we calculate the heat capacity numerically in the case of the simple square lattice. We fix the nearest-neighbor hopping to $t = 100$ meV, the electronic filling to $\langle n \rangle = 0.6$, and consider the critical temperatures $T_{c1} = 1.5$ K and $T_{c2} = 1.2$ K. For the order parameters, we consider the cases $s + id_{xy}$ and $d_{x^2-y^2} + ig_{xy(x^2-y^2)}$, and we employ the leading lattice harmonics for the individual components. As for the temperature dependence we use $\Delta_0(T)$ and $X(T)$ as derived in Appendix B 2 with Ginzburg-Landau parameters $\alpha_a^0 = \alpha_b^0 = 30$ meV^{-1} and $\beta_a = \beta_b = 1$ meV^{-3} fixed for simplicity. Fixing these parameters is done for illustrational purposes and to highlight the role of β_{ab}.

The results clearly confirm the two key points of Sec. II C: the second jump is suppressed if the least nodal component onsets first, and turning on β_{ab} reduces the second jump further. In the $s + id_{xy}$ case of Fig. 2(a), the second jump is strongly suppressed with $\beta_{ab} = 0.2\beta_a$, and it is practically unresolvable under the same conditions for $d_{x^2-y^2} + ig_{xy(x^2-y^2)}$ in Fig. 2(b). Note that for the order parameter components considered here the low-temperature tail is different for the two scenarios: since $s + id$ is fully gapped, $C(T)/T$ is exponentially suppressed below the full gap, whereas $d + ig$ has symmetry-imposed line nodes along the zone diagonal, making $C(T)/T \sim T$ at low temperatures.

III. CASE STUDY: Sr$_2$RuO$_4$

Combined heat capacity and muon spin relaxation (μSR) measurements have demonstrated that the onset of superconductivity and TRSB split under uniaxial (100) strain in Sr$_2$RuO$_4$ (SRO) [51]. If this splitting is directly linked to the splitting of the critical temperatures of two uniform order parameter components, one generically expects a second heat capacity jump at the lower temperature scale, i.e., the onset of TRSB. However, despite intensive efforts from high-resolution heat capacity measurements resolved under strain, no second transition is observed [27]. While the absence of a second jump possibly is caused by smearing at zero strain if the two temperatures are finely tuned [39], a second jump should in principle be resolvable under finite (100) strain. This conundrum is arguably one of the major outstanding puzzles regarding the superconducting state in Sr$_2$RuO$_4$.

Within recent spin-fluctuation based calculations for superconductivity in Sr$_2$RuO$_4$, it was demonstrated that including longer-range Coulomb interactions in the random phase approximation (RPA) renormalized susceptibility can result in a close competition between s' and d_{xy} solutions to the linearized gap equation, making an $s' + id_{xy}$ order parameter a microscopically viable candidate order parameter for Sr$_2$RuO$_4$ [35]. At face value, both accidentally degenerate possibilities $s' + id_{xy}$ and $d_{x^2-y^2} + ig_{xy(x^2-y^2)}$ appear consistent with the breaking of time-reversal symmetry [29,30] with absence of edge currents [23,52], as well as nuclear
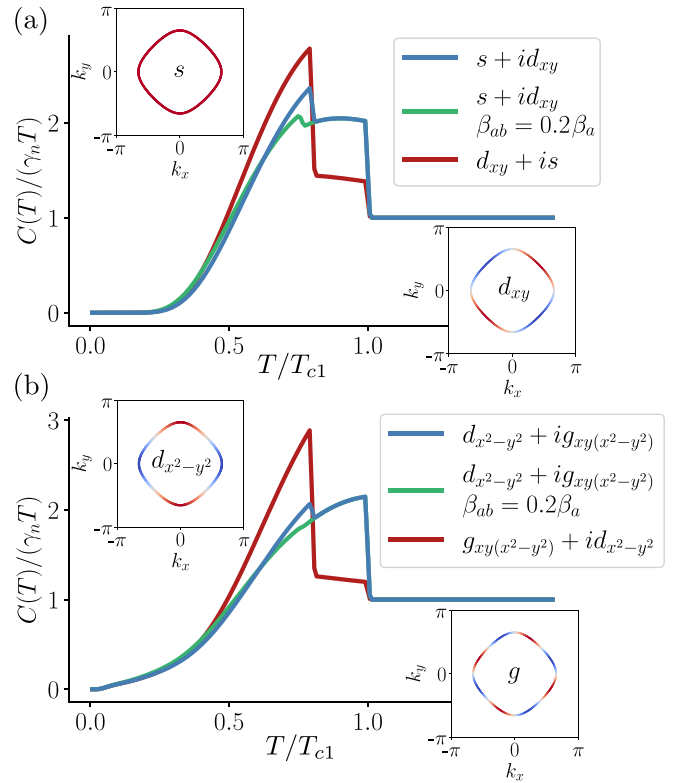

FIG. 2. Heat capacity for $s + id_{xy}$ [panel (a)] and $d_{x^2-y^2} + ig_{xy(x^2-y^2)}$ [panel (b)] order parameters per temperature per normal-state value in a one-band model. We consider the square lattice with nearest-neighbor hopping $t = 100$ meV at filling $\langle n \rangle = 0.6$, with critical temperatures $T_{c1} = 1.5$ K, $T_{c2} = 1.2$ K, and Ginzburg-Landau parameters fixed to $\alpha_a^0 = \alpha_b^0 = 30$ meV^{-1} and $\beta_a = \beta_b = 1$ meV^{-3}. We take $\beta_{ab} = 0$ (blue curves), $\beta_{ab} = 0.2\beta_a$ (green curves), and the opposite order of both components with $\beta_{ab} = 0$ (red curves), using the fundamental harmonic order parameters shown in the insets.

magnetic resonance [17,18], acoustic attenuation [31,32], scanning tunneling microscopy [25,53], and heat conductivity measurements [28]. However, it should be noted that several outstanding questions remain on how such accidentally degenerate pairing condensates relate to phase sensitive junction experiments [54–56], indirect observations of half-quantum vortices [57,58], and field-angle-dependent specific heat [59]. In addition, accidentally degenerate pairing states face the challenge to explain the missing second specific heat jump, as discussed above. It is this latter question that we further pursue here.

A. Band structure, order parameters, and transition temperatures

For the band structure we employ a 2D three-band tight-binding model describing the t_{2g} orbitals of the Ru atoms consistent with angular resolved photoemission spectroscopy (ARPES) measurements [60]. Uniaxial (100) strain is modeled by linear distortions, quantified by a dimensionless parameter p, of the hopping parameters using the experimentally determined Poisson's ratio [61,62]. In Fig. 3 we show the Fermi surface obtained from the tight-binding model, with
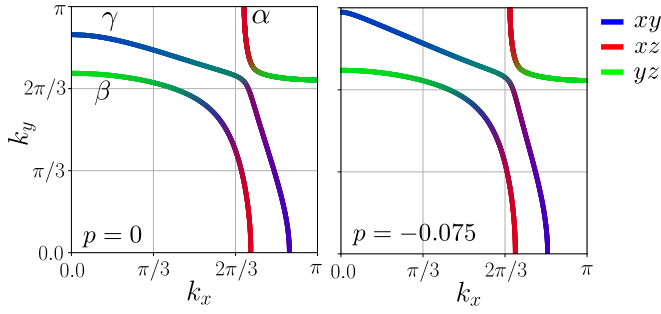
FIG. 3. Fermi surface from the three-band tight-binding model for Sr_2RuO_4 described in Appendix C. Left panel: Unstained case, and right panel: uniaxial (100) strain just below the Lifshitz transition on the γ band. The bands have been color coded by their Ru t_{2g} orbital content.

details listed in Appendix C. The left panel displays the unstrained band structure ($p = 0$), and the right panel shows the band structure subject to uniaxial (100) strain ($p = -0.075$) close to the van Hove point at which the γ band undergoes a Lifshitz transition.

As demonstrated in Ref. [35], for the parameter choice $U = 100$ meV (on-site Hubbard), $J/U = 0.1$ (Hund's coupling), and $V/U = 0.2$ (nearest-neighbor Hubbard), an $s' + id_{xy}$ solution can be stabilized as a function of V'/U, where V' is the next-nearest-neighbor interaction. In Fig. 4 we show the leading and nearly degenerate s' and d_{xy} solutions at zero and finite ($p = -0.05$) uniaxial (100) strain for $V' = 0$. The two components share momentum structure on large portions of the Fermi surface, and the combination $s' + id_{xy}$ has a near-node on the γ band that persists to finite strains; the position appears well correlated with where the orbital content changes from being dominated by d_{xy} to $d_{xz/yz}$ [35].
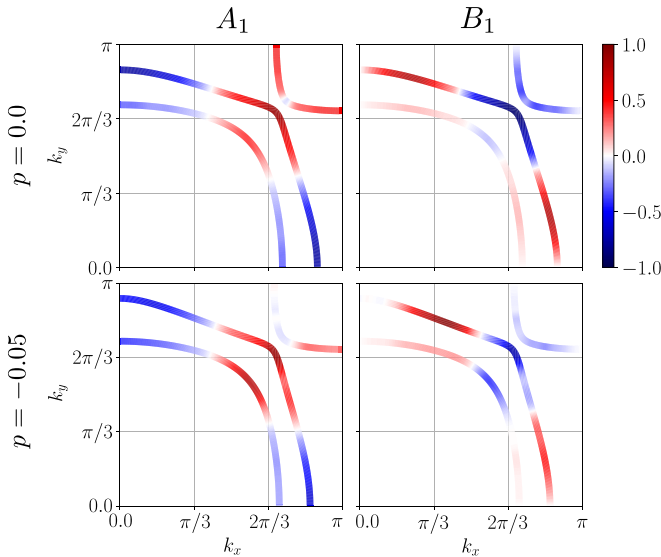

FIG. 4. Leading even-parity order parameters (labeled s' and d_{xy} at $p = 0$) belonging to irreducible representations A_1 and B_1 of the point group D_2 at zero and finite (100) uniaxial strain from the RPA calculations of Ref. [35]. The interaction parameters were set to $U = 100$ meV, $J/U = 0.1$, and $V/U = 0.2$.
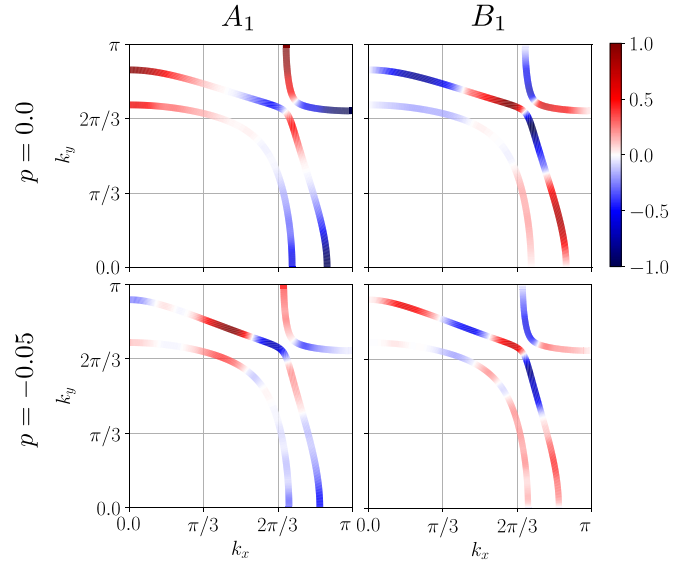

FIG. 5. Next-to-leading even-parity order parameters (labeled $d_{x^2-y^2}$ and $g_{xy(x^2-y^2)}$ at $p = 0$) belonging to irreducible representations A_1 and B_1 of the point group D_2 at zero and finite (100) uniaxial strain from the RPA calculations of Ref. [35] and for the same interaction parameters as in Fig. 4.

Similarly, in Fig. 5 we show the next-to-leading order parameters ($d_{x^2-y^2}$ and $g_{xy(x^2-y^2)}$) for the same interaction parameters. The next-to-leading orders share, by symmetry, a common node along the zone diagonals $k_x = \pm k_y$ in the unstrained case. This common node is lifted at finite in-plane strain. Supplementary plots of the order parameters are provided in Appendix D.

As mentioned above, combined heat capacity and μSR measurements have demonstrated that the onset of superconductivity and TRSB split under uniaxial (100) strain in Sr_2RuO_4 [51]. Theoretically, this result has been described as a strain-induced splitting of the leading superconducting instabilities [62]. In Fig. 6 we show the experimentally
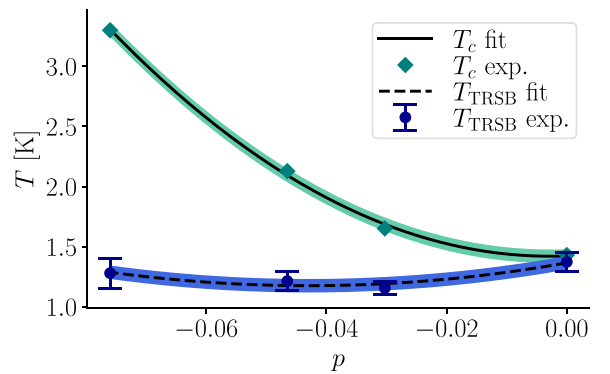

FIG. 6. Split transition temperatures as a function of the dimensionless uniaxial (100) strain parameter p, as measured with combined heat capacity (teal diamonds) and μSR (blue circles) from Ref. [51]. Gray lines are quadratic fits to the data points, used to parametrize $T_c(p)$ and $T_{TRSB}(p)$ as used in the calculations. The light blue and red colored bands indicate transition widths of $\sigma = 100$ mK; cf. the simulated smearing in Fig. 7.
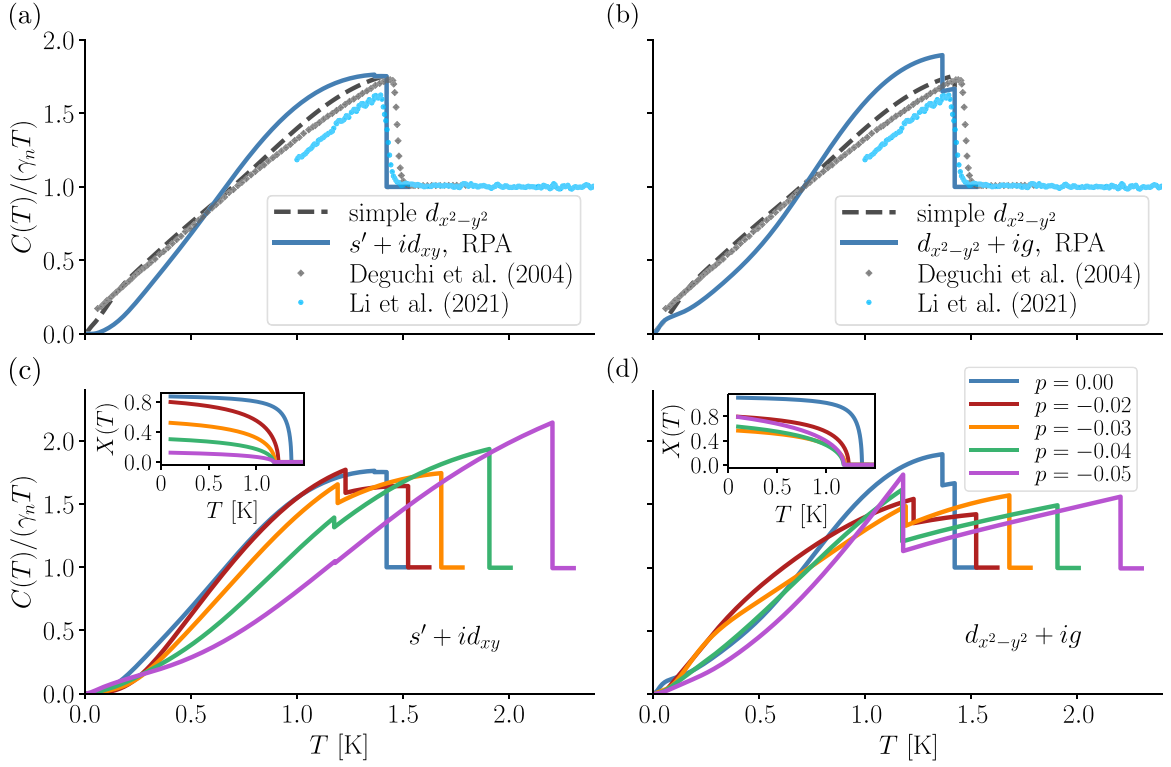
FIG. 7. Heat capacity per temperature and normal-state value for the (left column) $s' + id_{xy}$ and (right column) $d_{x^2-y^2} + ig_{xy(x^2-y^2)}$ order parameters from Ref. [35]. Panels (a) and (b): The unstrained case. We use (blue lines) the order parameters from Figs. 4 and 5 with $\Delta_0(T)$ and $X(T)$ (insets) that minimize the free energy of Eq. (8). The experimental data from Refs. [27,63] is plotted alongside. The black dashed line shows the result for a single-component $d_{x^2-y^2}$-wave order parameter, $\Delta_\mu(\boldsymbol{p}) = \Delta_\mu(\cos p_x - \cos p_y)$ with $\Delta_\alpha/\Delta_\gamma = 0.55$ and $\Delta_\beta/\Delta_\gamma = 0.45$, for reference. Panels (c) and (d): Calculated heat capacity at finite strain with $X(T)$ shown in the insets.

obtained transition temperatures, T_c and T_{TRSB}, as obtained from the primary heat capacity jump and the abrupt change in the muon spin relaxation rate, respectively. The data points have been fitted with quadratic polynomials after a linear rescaling of the strain axis such that the experimental van Hove strain of $\varepsilon_{xx} = -0.703$ GPa matches the dimensionless strain parameter $p = -0.076$.

B. Calculated specific heat transitions

Equipped with the band structure, order parameters, and transition temperatures of the preceding subsection, we numerically compute the Ginzburg-Landau coefficients of Eqs. (9)–(11) and minimize the free energy of Eq. (8) with respect to $\Delta_0(T)$ and $X(T)$ (see Appendix B 2 for the general expressions). Using the order parameter of Eq. (1) [64], we proceed by evaluating the heat capacity as a function of uniaxial (100) strain. Results are shown in Fig. 7 for both the $s' + id_{xy}$ [panels (a) and (c)] and the $d_{x^2-y^2} + ig_{xy(x^2-y^2)}$ [panels (b) and (d)] order parameters. We stress that labeling the order parameters by the D_4 harmonics, like $d_{x^2-y^2}$, is not strictly accurate notation; by s' we refer to the leading order parameter belonging to irrep A_1 of D_2, by d_{xy} we refer to the leading order in the B_1 channel, by $d_{x^2-y^2}$ we refer to the next-to-leading order in the A_1 channel, and by $g_{xy(x^2-y^2)}$ we refer to the next-to-leading order in the B_1 channel. For the five considered values of strain, $p = 0.0, -0.02, -0.03, -0.04, -0.05$, the numerical results for the heat capacity jump ratios are

summarized in Table I. As seen, the the second discontinuity is generally rather modest for the $s' + id_{xy}$ case, especially at zero strain where the jump is hardly visible in Fig. 7(a).

In Fig. 8 we show the simulated effect of smearing of the phase transition, which experimentally could originate from disorder or strain inhomogeneity. The smearing is modeled by averaging over 300 realizations with the transition temperatures drawn from normal distributions with mean given by the fits $T_c(p)$ and $T_{\mathrm{TRSB}}(p)$ in Fig. 6 and standard deviation of $\sigma = 100$ mK, respectively. In the experiment of Ref. [27], the width of the primary heat capacity jump varies around $\sigma = 30$–200 mK. The width of the jump initially increases with strain, before becoming sharper again at the largest values of the strain. This can be understood if the dominant source of the broadening is strain inhomogeneity: At intermediate strain, T_c changes fastest as a function of strain and therefore

TABLE I. Calculated ratios of specific heat jumps η extracted from the numerical results of Figs. 7(c) and 7(d).

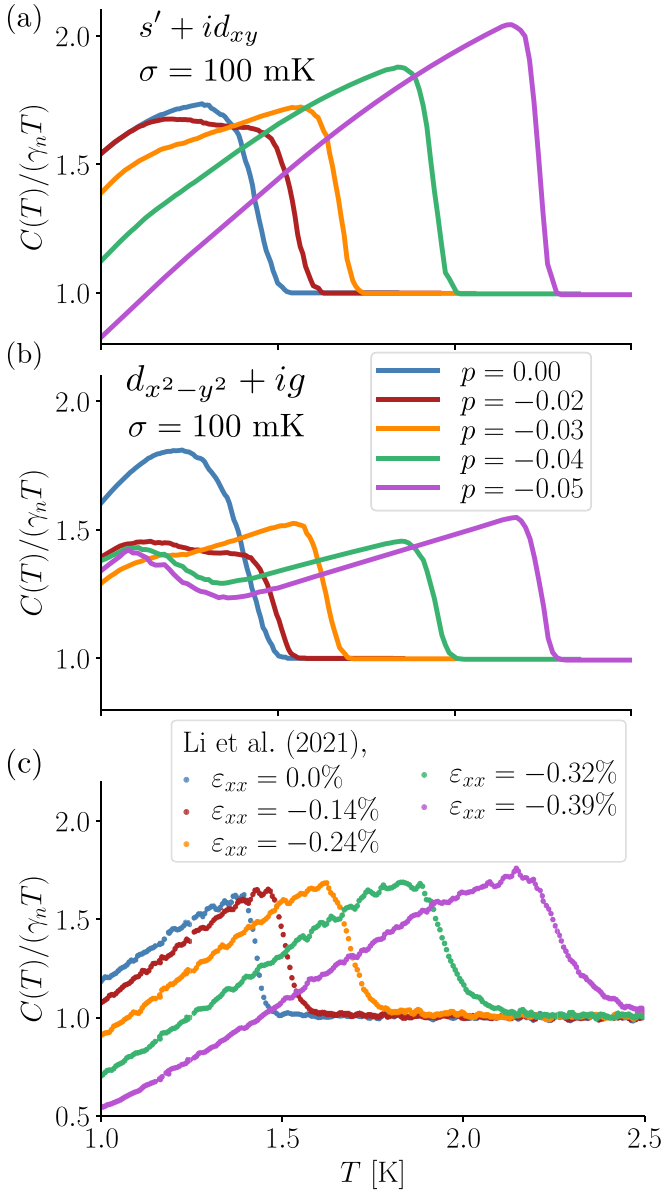| Strain p	Jump ratio $\eta_{s'+id}$	Jump ratio η_{d+ig}
0.0	0.014	0.369
−0.02	0.283	0.453
−0.03	0.198	0.269
−0.04	0.081	0.827
−0.05	0.012	0.938

FIG. 8. Simulated effect of smearing in the (a) $s' + id_{xy}$ and (b) $d_{x^2-y^2} + ig_{xy(x^2-y^2)}$ order parameter scenario for the same strain values as considered in Figs. 7(c) and 7(d). Smearing is here modeled by averaging over realizations where we draw transition temperatures from normal distributions with means $T_c(p)$ and $T_{TRSB}(p)$ from Fig. 6 and standard deviation $\sigma = 100$ mK. For each realization we calculate the Ginzburg-Landau coefficients of Eqs. (9)–(11) and obtain the heat capacity from Eq. (A6) with the order parameter of Eq. (1). Panel (c): The experimental data from Ref. [27], providing an indirect measurement of the heat capacity.

the effect of strain inhomogeneity is the most pronounced [27].

The effect of smearing is more easily understood in a toy model for the heat capacity (per temperature)

$$c(T, T_c) := aT[1 - \Theta(T - T_c)], \quad (15)$$

where Θ is the Heaviside function and a is the slope of c below T_c. If the step locations T_c are drawn from a normal

distribution with mean $\bar{T}_c$ and standard deviation σ, then

$$\lim_{N \to \infty} \frac{1}{N} \sum_{\{T_c\}} c(T, T_c) = \frac{1}{2} aT \left[1 - \text{Erf}\left(\frac{T - \bar{T}_c}{\sqrt{2}\sigma}\right)\right], \quad (16)$$

where Erf is the error function; the width of the smeared transition is straightforwardly controlled by σ. One may therefore expect a significantly smeared double transition when $T_c - T_{TRSB} \lesssim \sigma$. In Fig. 6 we have indicated widths of $\sigma = 100$ mK as colored bands around the transition temperatures.

C. Discussion

Considering the results of the unstrained material in the top panel of Fig. 7, neither order parameter candidate, $s' + id_{xy}$ or $d_{x^2-y^2} + ig_{xy(x^2-y^2)}$, provides a perfect match with the temperature dependence of the experimental data of Ref. [63]. However, given that we feed in microscopically computed form factors obtained from a specific set of parameters, we do not consider this discrepancy a fundamental concern. As demonstrated in Appendix D, the match to the experimental data can be improved by, e.g., redistributing the band-resolved gap magnitudes compared to the RPA solution.

Noticeably, in the unstrained case the second jump of the $s' + id_{xy}$ order is very tiny, and an order of magnitude smaller than for $d_{x^2-y^2} + ig_{xy(x^2-y^2)}$. Under uniaxial in-plane strain, the second jump is initially found to grow in the case of $s' + id_{xy}$ before decreasing again for strains $p < -0.02$. For $d_{x^2-y^2} + ig_{xy(x^2-y^2)}$ the second jump evolves differently with strain but remains sizable and outside the threshold for detection reported in Ref. [27].

The second jump evolving nonmonotonically under strain in both order parameter scenarios points to the importance of the A term in Eq. (3) since the simplified case of Eq. (14), in which the A term is absent, predicts a monotonic decrease of the second jump with strain. As noted before, the A term becoming sizable is linked to a shared momentum structure of the form factors. Accommodating a small second jump under strain thus requires the accidental nodes, which generally shift on the Fermi surface under strain, to shift in a similar fashion for the two form factor components, which is highly constraining and *a priori* implausible. Any failure of this synchronized node matching under strain can therefore be identified as an effect working against second jump reduction found in Eq. (14).

In both order parameter scenarios considered here, the A_1 and B_1 form factors exhibit accidental nodes in the vicinity of $k_x, k_y = \pi/3$ at zero strain. Figures 4 and 5 show that for s' and d_{xy} these nodes shift in a rather modest way with strain compared to $d_{x^2-y^2}$ and g; the latter two also develop additional nodal regions at the highest strains. It is also worth noting that the symmetry-protected zone-diagonal node in the $d_{x^2-y^2} + ig_{xy(x^2-y^2)}$ scenario is lifted for finite strain, which can be seen in the low-temperature tail in Fig. 7(d). We attribute the dissimilar behavior of the second jump under strain of $s' + id_{xy}$ vs $d_{x^2-y^2} + ig_{xy(x^2-y^2)}$ to this different strain-induced node shifting.

When smearing is added in Fig. 8, it is seen that a smearing width of $\sigma = 100$ mK is enough to bring the second jump

into the undetectable regime for the $s' + id_{xy}$ case; a case with 50 mK smearing is shown Appendix. D. In contrast, the second jump remains clearly resolvable for $d_{x^2-y^2} + ig_{xy(x^2-y^2)}$. When comparing to the experimental data of Ref. [27], shown in Fig. 8(c) for completeness, we conclude that $s' + id_{xy}$ is a more likely order parameter candidate than $d_{x^2-y^2} + ig_{xy(x^2-y^2)}$ within the premises of our calculation. We also note that the results change drastically if one instead considers the reversed combination of orders, e.g., $d_{xy} + is'$ as opposed to $s' + id_{xy}$. In Appendix D we show results for the $d_{xy} + is'$ case, which results in $\eta \geqslant 0.26$. Thus, as noted in Sec. II C, the order in which the order parameters switch on has a large impact on the heat capacity jumps. The order parameter combination $s' + id_{xy}$ where the s' order condenses at the higher temperature has a small second jump, whereas the $d_{xy} + is'$ combination has a large second jump and can therefore be ruled out.

Among the aforementioned order parameter candidates recently proposed for Sr_2RuO_4 we have so far not addressed the $d_{xz} + id_{yz}$ state (E_g irrep of D_{4h}) [33,34]. Although this order parameter cannot be accessed with a two-dimensional model for the band structure, we note that previous microscopic three-dimensional models have found this state unfavorable [20,38,49]. Yet, based on the principles regarding the size of the second heat capacity jump in Sec. II, we can infer general expectations for split transitions in the case of two-dimensional irreps, even though the quantitative result comes down to details of the specific order parameters considered. Note that if the two components are degenerate by symmetry, the perturbation ϵ that causes their splitting must break the crystal symmetries, like uniaxial (100) strain in tetragonal systems. Besides the symmetry-imposed horizontal line node at $k_z = 0$ of $d_{xz} + id_{yz}$, the vertical symmetry-imposed nodes of the two components, i.e., at $k_x = 0$ and $k_y = 0$, are maximally shifted which from the principles of Sec. II C is expected to give a sizable second jump. Furthermore, since the sizes of the two components are equal in the unperturbed case by symmetry ($X = 1$), the two transitions are naively expected to be associated with equally sized heat capacity jumps, at least close to the unperturbed case (cf. supplemental Fig. S9 of Ref. [27]). Thus, based on these considerations alone, the $d_{xz} + id_{yz}$ scenario for Sr_2RuO_4 appears less likely than the accidentally degenerate cases of $s' + id_{xy}$ and $d_{x^2-y^2} + ig_{xy(x^2-y^2)}$.

Contrasting the focus on exotic multicomponent orders relying on accidental degeneracies, the simpler explanation of the specific heat data of Sr_2RuO_4 in terms of a single $d_{x^2-y^2}$ order parameter should not be dismissed (cf. the gray dashed line in Fig. 7). As discussed above, however, this possibility raises the immediate question of how to explain, e.g., the ultrasound experiments and the evidence of TRSB [29,31,32,45]. Regarding the latter, since Sr_2RuO_4 resides in the vicinity of magnetic instabilities [46] perhaps TRSB is related to glassy pinned magnetism or coupling between magnetic and superconducting orders [65,66]. Another possibility is that there is a second inhomogeneous order parameter component that is induced by sample dislocations, which is also expected to result in a small second jump [37].

IV. OTHER TIME-REVERSAL SYMMETRY BROKEN SUPERCONDUCTORS

In the heavy-fermion compound UPt_3 there is convincing experimental evidence of a two-component order parameter deep in the superconducting phase. Two distinct transition temperatures are revealed by two jumps visible in the ultrasound velocity as a function of temperature [67]. Furthermore, TRSB is observed at temperatures below the second transition. The Kerr effect has been observed [68], indicating TRSB below $T_{TRSB} \approx 0.46$ K, while the critical temperature as measured by the drop in the resistance is $T_c \approx 0.55$ K. In addition, TRSB is also seen in a μSR signal [69] (although we should caution that an independent μSR experiment failed to see any signature of TRSB [70]). A likely order parameter candidate is $f_{z(x^2-y^2)} + if_{xyz}$ [5,71] (where the degeneracy of the two-dimensional irrep is split by magnetism). In UPt_3 a very clear second heat capacity jump is observed [72]. The Fermi surface of UPt_3 is complicated and contains five strongly three-dimensional sheets when the $5f$ uranium electrons are included [73]. For the $f_{z(x^2-y^2)} + if_{xyz}$ scenario, modulo all the details of the multiband fermiology and possible accidental nodes, the vertical symmetry-imposed nodes are maximally shifted when comparing the two components, which, according to Sec. II C, suggests that one can expect equally sized heat capacity jumps. On the phenomenological level this agrees with what is observed experimentally [72,74].

UTe_2 has attracted significant attention recently as an unconventional superconductor. The Kerr effect indicating TRSB has been observed [75]. However, a second heat capacity jump is only observed under hydrostatic pressure [42,76] while no second jump is seen under applied stress [77]. It is hypothesized that the presence or absence of the second jump may be affected by sample quality [78]. UTe_2 has an orthorhombic structure (D_{2h}) and its Fermi surface, although not fully characterized, is understood to be fully three-dimensional [7]. A large upper critical field indicates that UTe_2 is a spin-triplet superconductor and different order parameter combinations that have been proposed include $A_{1u} + iB_{3u}$ [79], $B_{1u} + iB_{2u}$ [80], and $B_{2u} + iB_{3u}$ [75]. In all three cases, the order parameters have different momentum space structure and quasiparticles are gapped out at the second transition, implying that all three order parameter combinations are consistent with a large second heat capacity jump.

Another material relevant for multicomponent superconductivity is UBe_{13}. In this material, a second heat capacity jump is observed under doping of UBe_{13} to $U_{1-x}Th_xBe_{13}$ [81]. μSR experiments observe TRSB consistent with either TRSB superconductivity or with antiferromagnetism coexisting with superconductivity [82]. Note that the μSR transition coincides with the second heat capacity jump, implying they have a common origin. In more recent experiments [83] two heat capacity jumps were clearly seen as well, and furthermore the low-temperature phase was shown to be fully gapped. This led the authors to propose two different candidates for the two orders. The symmetry group is the cubic space group O_h which has a two-dimensional irrep E_u with the basis functions $\boldsymbol{d}_1(k) = \sqrt{3}(k_x\hat{x} - k_y\hat{y})$ and $\boldsymbol{d}_2(k) = -k_x\hat{x} - k_y\hat{y} + 2k_z\hat{z}$.

Assuming the degeneracy between the two orders to be lifted with d_1 switching on at a higher temperature, we expect a large heat capacity jump since d_1 has a line node, whereas $d_1 + id_2$ only has a point node, leading to a significant number of quasiparticles being gapped out at the second transition. The second scenario proposed by the authors considers an accidental degeneracy of A_{1u} and A_{2u}; A_{1u} is already fully gapped and therefore based on our formalism we would expect a smaller second jump for the candidate $A_{1u} + iA_{2u}$, making this a less likely candidate.

Finally, TRSB has been also observed in $PrOs_4Sb_{12}$, which has a tetrahedral crystal symmetry T_h [84], via μSR experiments [16,85]. A clear second heat capacity jump is observed [86,87]. Thermal conductivity measurements indicate the presence of nodes or near-nodes in the high-temperature phase and this has lead to the proposal of an $s + id_{z^2-x^2}$ order parameter [84], where the s-wave order is highly anisotropic and features near-nodes. This could then also lead to a large second heat capacity jump and indeed theoretical calculations suggest that the second jump would be of the same size as the first one for this order parameter [84].

V. CONCLUSIONS

We have provided a general theoretical framework for the specific heat transitions in multicomponent time-reversal symmetry broken superconductors. This allowed a thorough discussion of the amplitudes of the specific heat jumps at the two transition temperatures. Specifically, one expects comparable specific heat discontinuities for most two-dimensional irreps due to the maximally misaligned nodes and the symmetry-imposed equality of order parameter component magnitudes. On the other hand, a significantly reduced second jump may be expected for TRSB superconductors that have competing order parameter components with similar momentum structure, and where the least nodal component onsets first. We applied the theoretical setup to perform a comprehensive discussion of the low-temperature electronic specific heat relevant for Sr_2RuO_4. While the specific heat data alone for this material are most straightforwardly explained by a nodal single-component superconductor, several other experimental probes point to TRSB multicomponent superconductivity [29,31,32,45]. We have pursued the accidentally degenerate possibilities $s' + id_{xy}$ and $d_{x^2-y^2} + ig_{xy(x^2-y^2)}$ with gap structures obtained from microscopic RPA calculations, and compared their specific heat behavior with experimental data in both the absence and presence of uniaxial strain. Our results yield a better agreement between experimental data and $s' + id_{xy}$ order, as compared to $d_{x^2-y^2} + ig_{xy(x^2-y^2)}$ superconductivity. Further, we conclude from these calculations that the currently available experimental specific heat data are consistent with $s' + id_{xy}$ superconductivity in the unstrained case, and also with the uniaxially strained data when considering the role of strain inhomogeneity.

ACKNOWLEDGMENTS

APPENDIX A: HEAT CAPACITY OF SUPERCONDUCTORS

The specific heat for a multiband superconductor follows from the expression for the entropy of the fermion gas [40],

$$S = -2k_B \sum_{\boldsymbol{k},\mu} (n_F[E_\mu(\boldsymbol{k})] \ln n_F[E_\mu(\boldsymbol{k})]$$
$$+ \{1 - n_F[E_\mu(\boldsymbol{k})]\} \ln \{1 - n_F[E_\mu(\boldsymbol{k})]\}). \quad (A1)$$

Here, $E_\mu(\boldsymbol{k}) = \sqrt{\xi_\mu^2 + |\Delta_\mu(T,\boldsymbol{k})|^2}$, and $n_F(E) = [1 + \exp(\beta E)]^{-1}$ is the Fermi function.

1. Single-component order parameter

We first assume a single-component order parameter with temperature dependence $\Delta(T)$,

$$\Delta_\mu(T,\boldsymbol{k}) = \Delta(T) f_\mu(\boldsymbol{k}), \quad (A2)$$

where $f_\mu(\boldsymbol{k})$ is the order parameter form factor of band μ normalized such that $\max_{\boldsymbol{k},\mu} |f_\mu(\boldsymbol{k})| = 1$. The specific heat follows from

$$C(T) = T\frac{\partial S}{\partial T} = 2\sum_{\boldsymbol{k},\mu} E_\mu(\boldsymbol{k})\frac{dn_F[E_\mu(\boldsymbol{k})]}{dT}$$

$$= \frac{2}{k_B T^2} \int_{-\infty}^\infty d\xi_\mu$$

$$\times \left\langle \frac{\xi_\mu^2 + \Delta(T)^2|f_\mu(\boldsymbol{k})|^2 - \frac{T}{2}\frac{\partial\Delta(T)^2}{\partial T}|f_\mu(\boldsymbol{k})|^2}{4\cosh^2\left(\frac{E_\mu(\boldsymbol{k})}{2k_B T}\right)} \right\rangle_{\text{FS}}, \quad (A3)$$

where the Fermi surface average is evaluated as

$$\langle A\rangle_{\text{FS}} := \sum_\mu \int_{S_\mu} \frac{d\boldsymbol{k}}{(2\pi)^d} \frac{A}{v_\mu(\boldsymbol{k})}, \quad (A4)$$

where $v_\mu(\boldsymbol{k}) = |\nabla\xi_\mu(\boldsymbol{k})|$ is the Fermi velocity and $\rho_\mu = \frac{1}{(2\pi)^d}\int_{S_\mu} d\boldsymbol{k}/v_\mu(\boldsymbol{k})$ is the density of states of band μ.

By evaluating Eq. (A3) in the normal state, for which $\Delta = 0$, the specific heat per temperature, i.e., the Sommerfeld coefficient γ_n, becomes

$$\gamma_n := \frac{C_n(T)}{T} = \frac{2}{k_B T^3}\sum_\mu \rho_\mu \int_{-\infty}^\infty d\xi \frac{\xi^2}{4\cosh^2\left(\frac{\xi}{2k_B T}\right)}$$

$$= 4k_B^2\zeta(2)\sum_\mu \rho_\mu, \quad (A5)$$

with $\zeta(2) = \pi^2/6$. This recovers the multiband version of the well-known (electronic) linear contribution to the specific heat
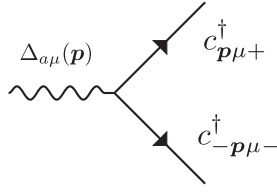
FIG. 9. Cooper pair operator in the (pseudo)spin singlet channel.

of a metal [40]. It is convenient to normalize Eq. (A3) by the normal-state value:

$$
\frac{C(T)}{T\gamma_n} = \frac{3}{4\pi^2(k_BT)^3\sum_b\rho_b}\int_{-\infty}^{\infty}d\xi
$$
$$
\times\left\langle\frac{\xi^2+\Delta(T)^2|f_\mu(\mathbf{k})|^2-\frac{T}{2}\frac{\partial\Delta(T)^2}{\partial T}|f_\mu(\mathbf{k})|^2}{\cosh^2\left(\frac{E_\mu(\mathbf{k})}{2k_BT}\right)}\right\rangle_{\text{FS}}.
$$

(A6)

2. Two-component order parameter with simple temperature dependence

Following Ref. [36] we assume a TRSB two-component order parameter with the particular BCS-like temperature dependence

$$
\Delta(\mathbf{p}) = \Delta_{0,a}\sqrt{1-\frac{T}{T_c}}f_a(\mathbf{p}) + i\Delta_{0,b}\sqrt{1-\frac{T}{T_{\text{TRSB}}}}f_b(\mathbf{p}),
$$

(A7)

where a and b are irrep labels. We shall use this ansatz in Eq. (A3) and evaluate the heat capacity jump across T_c and T_{TRSB}. At the onset of superconductivity we get

$$
\frac{\Delta C_{\text{SC}}}{T_c} := \frac{C(T\to T_c^-)-C(T\to T_c^+)}{T_c}
$$
$$
= \frac{1}{T_c}\left(\frac{\Delta_{0,a}}{k_BT_c}\right)^2\langle|f_a(\mathbf{p})|^2\rangle_{\text{FS}}\int_{-\infty}^{\infty}\frac{d\xi}{4\cosh^2\left(\frac{\xi}{2k_BT_c}\right)}
$$
$$
= k_B\left(\frac{\Delta_{0,a}}{k_BT_c}\right)^2\langle|f_a(\mathbf{p})|^2\rangle_{\text{FS}},
$$

(A8)

where the only contribution we pick up comes from the third term in the numerator of Eq. (A3), due to its discontinuity at T_c. Repeating the calculation at the onset of the second order parameter component we now get

$$
\frac{\Delta C_{\text{TRSB}}}{T_{\text{TRSB}}} := \frac{C(T\to T_{\text{TRSB}}^-)-C(T\to T_{\text{TRSB}}^+)}{T_{\text{TRSB}}}
$$
$$
= k_B\left(\frac{\Delta_{0,b}}{k_BT_{\text{TRSB}}}\right)^2\left\langle|f_b(\mathbf{p})|^2\right.
$$
$$
\times\int_0^{\infty}\frac{du}{\cosh^2\left(\sqrt{u^2+z(\mathbf{p})^2}\right)}\right\rangle_{\text{FS}},
$$

(A9)

where $z(\mathbf{p}) = \frac{\Delta_{0,a}}{2k_BT_{\text{TRSB}}}\sqrt{1-\frac{T_{\text{TRSB}}}{T_c}}f_a(\mathbf{p})$ was introduced. Combining these two expressions we get the ratio of the heat

capacity jumps

$$
\eta := \frac{\Delta C_{\text{TRSB}}/T_{\text{TRSB}}}{\Delta C_{\text{SC}}/T_c} = \left(\frac{\Delta_{0,b}}{\Delta_{0,a}}\frac{T_c}{T_{\text{TRSB}}}\right)^2\frac{\langle|f_b(\mathbf{p})|^2\mathcal{I}[z(\mathbf{p})]\rangle_{\text{FS}}}{\langle|f_a(\mathbf{p})|^2\rangle_{\text{FS}}},
$$

(A10)

where

$$
\mathcal{I}(z) := \int_0^{\infty}du\cosh^{-2}(\sqrt{u^2+z^2}).
$$

(A11)

We note that this function for small z can be approximated as $\mathcal{I}(z) = 1 - \frac{7\zeta(3)}{\pi^2}z^2 + O(z^4) \approx \exp(-\frac{7\zeta(3)}{\pi^2}z^2)$.

3. Two-component order parameter with general temperature dependence

We go beyond the square root ansatz in Eq. (A7) by assuming

$$
\Delta(T,\mathbf{p}) = \Delta_0(T)[f_a(\mathbf{p}) + iX(T)f_b(\mathbf{p})].
$$

(A12)

Above we have left band indices on $f_{a/b}(\mathbf{p})$ implicit. Crucially, this ansatz allows for the two components to interact in the sense that $\Delta_0(T)$ can, and generally will, be nonanalytic at $T = T_{\text{TRSB}}$ where X onsets. This also results in two terms being picked up in the numerator of η, coming from

$$
A := \left[\frac{\partial\Delta_0(T)^2}{\partial T}\bigg|_{T\to T_{\text{TRSB}}^-} - \frac{\partial\Delta_0(T)^2}{\partial T}\bigg|_{T\to T_{\text{TRSB}}^+}\right]\bigg/D
$$

(A13)

and

$$
B := \left[\frac{\partial[\Delta_0(T)X(T)]^2}{\partial T}\bigg|_{T\to T_{\text{TRSB}}^-}\right.
$$
$$
\left. - \frac{\partial[\Delta_0(T)X(T)]^2}{\partial T}\bigg|_{T\to T_{\text{TRSB}}^+}\right]\bigg/D,
$$

(A14)

with $D := \frac{\partial\Delta_0(T)^2}{\partial T}|_{T\to T_c^-} - \frac{\partial\Delta_0(T)^2}{\partial T}|_{T\to T_c^+}$, respectively. Repeating the calculation of Sec. A 2 now results in

$$
\eta = \frac{T_c}{T_{\text{TRSB}}}\left(A\frac{\langle|f_a(\mathbf{p})|^2\mathcal{I}[z(\mathbf{p})]\rangle_{\text{FS}}}{\langle|f_a(\mathbf{p})|^2\rangle_{\text{FS}}} + B\frac{\langle|f_b(\mathbf{p})|^2\mathcal{I}[z(\mathbf{p})]\rangle_{\text{FS}}}{\langle|f_a(\mathbf{p})|^2\rangle_{\text{FS}}}\right),
$$

(A15)

with $z(\mathbf{p}) = \frac{\Delta_0(T_{\text{TRSB}})}{2k_BT_{\text{TRSB}}}f_a(\mathbf{p})$.

APPENDIX B: MICROSCOPIC GINZBURG-LANDAU THEORY

In this Appendix we summarize the derivation of the microscopic Ginzburg-Landau theory of Ref. [39].

1. Derivation

We start with an electronic normal-state description,

$$
H_0 = \sum_{\mu,\sigma,\mathbf{p}}\xi_\mu(\mathbf{p})c_{\mathbf{p}\mu\sigma}^\dagger c_{\mathbf{p}\mu\sigma},
$$

(B1)

where, $\xi_\mu(\mathbf{p})$ is the dispersion of band μ, and $\sigma = +, -$ denotes (pseudo)spin (with $\bar{\sigma} = -\sigma$). We here consider the pseudospin-singlet Cooper pairs and treat H_{SC} as a perturbation to H_0 close to the critical temperature, where

$$
H_{\text{SC}} = \sum_{\mu,\sigma,a,\mathbf{p}}[\Delta_{a\mu}(\mathbf{p})c_{\mathbf{p}\mu\sigma}^\dagger c_{-\mathbf{p}\mu\bar{\sigma}}^\dagger + \text{H.c.}].
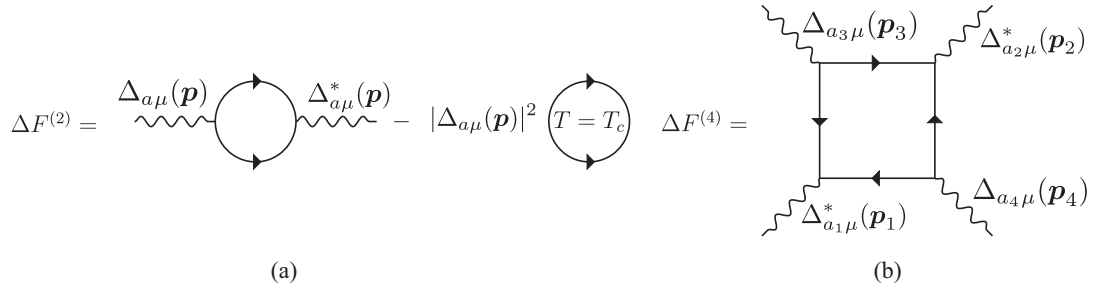$$

(B2)

FIG. 10. The (a) second-order and (b) fourth-order diagrams contributing to the free energy of Eq. (B3). Corresponding algebraic expressions are given by Eqs. (B6) and (B7).

Here $\Delta_{a\mu}(\boldsymbol{p})$ is the order parameter on band μ with symmetry label (irreducible representation) a. The sum over $\boldsymbol{p}$ runs over the Fermi surface sheet μ such that $|\xi_\mu(\boldsymbol{p})| < \omega_c \sim k_B T$, where $\omega_c \ll W$ is the momentum cutoff and W the bandwidth. Following the Ginzburg-Landau procedure, the free-energy corrections to the normal state, $\Delta F = F_{\text{SC}} - F_n$, are formally obtained by the Gibbs average [41,88]

$$\Delta F = -T \ln \left\langle \mathcal{T}_\tau \exp\left[-\int_0^\beta d\tau \, H_{\text{SC}}(\tau) \right] \right\rangle, \quad \text{(B3)}$$

where $\beta = 1/T$ (with $k_B = 1$), $\tau = -it$ is imaginary time, and $\mathcal{T}_\tau$ is the time-ordering operator. In the loop expansion of ΔF we sum consistently connected diagrams, constructed from the Cooper operator of Fig. 9, to a given order. To quartic order we have the diagrams of Fig. 10. The second- and quartic-order terms, $\Delta F = \Delta F^{(2)} + \Delta F^{(4)}$, are algebraically given by

$$\Delta F^{(2)} = \sum_{\mu, a, \boldsymbol{p}} \alpha_{a\mu}(\boldsymbol{p}, T) |\Delta_{a\mu}(\boldsymbol{p})|^2, \quad \text{(B4)}$$

$$\Delta F^{(4)} = \sum_{\mu, \{a_i\}, \{\boldsymbol{p}_i\}} \beta_{\{a_i\}\mu}(\{\boldsymbol{p}_i\}, T) \Delta_{a_1\mu}^*(\boldsymbol{p}_1)$$
$$\times \Delta_{a_2\mu}^*(\boldsymbol{p}_2) \Delta_{a_3\mu}(\boldsymbol{p}_3) \Delta_{a_4\mu}(\boldsymbol{p}_4), \quad \text{(B5)}$$

$$\alpha_{a\mu}(\boldsymbol{p}, T) = -T \sum_n G_\mu(\boldsymbol{p}, \omega_n) G_\mu(-\boldsymbol{p}, -\omega_n)$$
$$+ T_{ca} \sum_n G_\mu(\boldsymbol{p}, \omega_n) G_\mu(-\boldsymbol{p}, -\omega_n)|_{T=T_{ca}}, \quad \text{(B6)}$$

$$\beta_{\{a_i\}\mu}(\{\boldsymbol{p}_i\}, T) = \frac{T}{2} g_{a_1 a_2 a_3 a_4} \delta_{\boldsymbol{p}_1 \boldsymbol{p}_3} \delta_{\boldsymbol{p}_1 \boldsymbol{p}_4} \delta_{\boldsymbol{p}_2 \boldsymbol{p}_3} \delta_{\boldsymbol{p}_2 \boldsymbol{p}_4}$$
$$\times \sum_n G_\mu(\boldsymbol{p}_1, \omega_n) G_\mu(\boldsymbol{p}_2, \omega_n)$$
$$\times G_\mu(-\boldsymbol{p}_3, -\omega_n) G_\mu(-\boldsymbol{p}_4, -\omega_n), \quad \text{(B7)}$$

$$g_{a_1 a_2 a_3 a_4} := \delta_{a_1 a_3} \delta_{a_2 a_4} + \delta_{a_1 a_4} \delta_{a_2 a_3} + \delta_{a_1 a_2} \delta_{a_3 a_4}$$
$$- 2 \delta_{a_1 a_2} \delta_{a_2 a_3} \delta_{a_3 a_4}. \quad \text{(B8)}$$

Above, the Green's functions $G_\mu(\boldsymbol{p}, \omega_n) = 1/[i\omega_n - \xi_\mu(\boldsymbol{p})]$ with fermionic Matsubara frequencies $\omega_n = \frac{\pi}{\beta}(2n+1)$ for integer n were introduced. Next, we factorize the order parameter as $\Delta_{a\mu}(\boldsymbol{p}) = \Delta_{0a} f_{a\mu}(\boldsymbol{p})$, with $f_{a\mu}(\boldsymbol{p})$ being a (real)

normalized form factor, and Δ_{0a} is a (complex) variational parameter. The above equations simplify to

$$\Delta F = \Delta F^{(2)} + \Delta F^{(4)} = \sum_a \tilde{\alpha}_a(T, T_{ca}) |\Delta_{0a}|^2$$
$$+ \sum_{\{a_i\}} \tilde{\beta}_{\{a_i\}}(T_c) \Delta_{0a_1}^* \Delta_{0a_2}^* \Delta_{0a_3} \Delta_{0a_4}, \quad \text{(B9)}$$

$$\tilde{\alpha}_a(T, T_{ca}) = -V \sum_\mu \int \frac{d\boldsymbol{p}}{(2\pi)^d} \left(\frac{\tanh[\xi_\mu(\boldsymbol{p})/(2T)]}{2\xi_\mu(\boldsymbol{p})} - \frac{\tanh[\xi_\mu(\boldsymbol{p})/(2T_{ca})]}{2\xi_\mu(\boldsymbol{p})} \right) f_{a\mu}^2(\boldsymbol{p}), \quad \text{(B10)}$$

$$\tilde{\beta}_{\{a_i\}}(T) = g_{a_1 a_2 a_3 a_4} \frac{V}{2T^3} \sum_\mu \int \frac{d\boldsymbol{p}}{(2\pi)^d} h(\xi_\mu(\boldsymbol{p})/T)$$
$$\times f_{a_1\mu}(\boldsymbol{p}) f_{a_2\mu}(\boldsymbol{p}) f_{a_3\mu}(\boldsymbol{p}) f_{a_4\mu}(\boldsymbol{p}), \quad \text{(B11)}$$

after performing the Matsubara sums. Above, V is the unit cell volume, the momentum-dependent order parameter components are without loss of generality assumed real, and

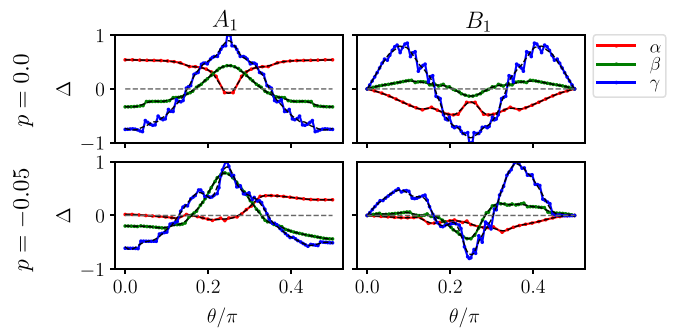$$h(x) := \frac{\sinh x - x}{4x^3(1 + \cosh x)}. \quad \text{(B12)}$$

FIG. 11. Order parameters from Fig. 4 labeled by the respective irreps of D_2, as a function of polar angle [on the α band the polar angle is measured from (π, π)]. The colored data points are the raw data from Ref. [35], and the black dashed lines show the data passed through a Savitzky-Golay filter to reduce finite-size effects. The filtered order parameters were used in the calculations of Sec. III B.
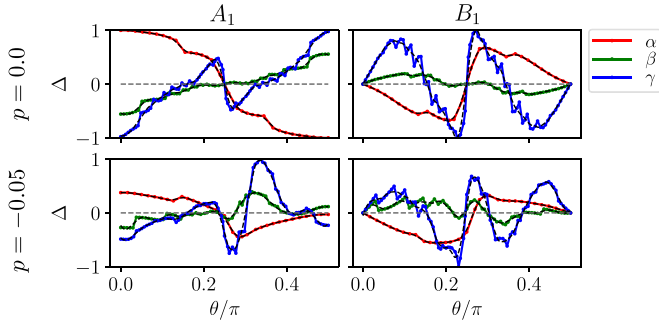
FIG. 12. Order parameters from Fig. 5 labeled by the respective irreps of D_2. See the caption of Fig. 11 for further details.

2. Minimization in the two-component case

In the two-component case of Eq. (1) the free energy of Eq. (8) is minimized over $X(T)$ and $\Delta_0(T)$. When redefining $\tilde{\alpha}_j \to \alpha_j$ and $\tilde{\beta}_j \to \beta_j$ for notational convenience, we get

$$X^2(T) = \begin{cases} \frac{\alpha_a(T)\beta_{ab} - \alpha_b(T)\beta_a}{\alpha_b(T)\beta_{ab} - \alpha_a(T)\beta_b}, & \text{for } T < T_{\text{TRSB}}, \\ 0, & \text{for } T > T_{\text{TRSB}}, \end{cases} \quad \text{(B13)}$$

and

$$\Delta_0^2(T) = \begin{cases} -\frac{1}{2}\frac{\alpha_b(T)\beta_{ab} - \beta_b\alpha_a(T)}{\beta_{ab}^2 - \beta_b\beta_a}, & \text{for } T < T_{\text{TRSB}}, \\ -\frac{\alpha_a(T)}{2\beta_a}, & \text{for } T_{\text{TRSB}} < T < T_c, \\ 0, & \text{for } T > T_c. \end{cases} \quad \text{(B14)}$$

After making the approximations $\alpha_a = \alpha_a^0(\frac{T}{T_{c1}} - 1)$ and $\alpha_b = \alpha_b^0(\frac{T}{T_{c2}} - 1)$, with $T_{c2} < T_{c1}$, the temperature T_{TRSB} is given by

$$T_{\text{TRSB}}(T_{c1}, T_{c2}) = T_{c2}\frac{1 - \frac{\beta_{ab}\alpha_a^0}{\beta_a\alpha_b^0}}{1 - \frac{T_{c2}}{T_{c1}}\frac{\beta_{ab}\alpha_a^0}{\beta_a\alpha_b^0}} < T_{c2}. \quad \text{(B15)}$$

For convenience we also introduce the temperature

$$T_*(T_{c1}, T_{c2}) = T_{c1}\frac{1 - \frac{\beta_{ab}\alpha_b^0}{\beta_b\alpha_a^0}}{1 - \frac{T_{c1}}{T_{c2}}\frac{\beta_{ab}\alpha_b^0}{\beta_b\alpha_a^0}} > T_{c1}, \quad \text{(B16)}$$

such that

$$\Delta_0^2(T < T_{\text{TRSB}}) = -\frac{1}{2}\frac{\beta_b\alpha_a^0 - \beta_{ab}\alpha_b^0}{\beta_{ab}^2 - \beta_a\beta_b}\left(1 - \frac{T}{T_*}\right)$$
$$= \Delta_0^2(0)\left(1 - \frac{T}{T_*}\right) \quad \text{(B17)}$$

and

$$X^2(T < T_{\text{TRSB}}) = \frac{\beta_{ab}\alpha_a^0 - \beta_a\alpha_b^0}{\beta_{ab}\alpha_b^0 - \alpha_a^0\beta_b}\frac{1 - \frac{T}{T_{\text{TRSB}}}}{1 - \frac{T}{T_*}}$$
$$= X^2(0)\frac{1 - \frac{T}{T_{\text{TRSB}}}}{1 - \frac{T}{T_*}}. \quad \text{(B18)}$$

APPENDIX C: THREE-BAND TIGHT-BINDING MODEL FOR Sr$_2$RuO$_4$

We employ an effective 2D three-band model for the band structure of Sr$_2$RuO$_4$,

$$H_0 = \sum_{k,s} \boldsymbol{\psi}_s^\dagger(\boldsymbol{k}) h_s(\boldsymbol{k}) \boldsymbol{\psi}_s(\boldsymbol{k}), \quad \text{(C1)}$$

where $\boldsymbol{\psi}_s(\boldsymbol{k}) = [c_{xz,s}(\boldsymbol{k}),\ c_{yz,s}(\boldsymbol{k}),\ c_{xy,-s}(\boldsymbol{k})]^T$ and where $s \in \{\uparrow, \downarrow\}$ denotes spin and $a \in \{xz, yz, xy\}$ denotes the d orbitals of the Ru atoms, which are relevant close to the Fermi energy. For $h_s(\boldsymbol{k})$ we take

$$h_s(\boldsymbol{k}) = \begin{pmatrix} \varepsilon_{xz}(\boldsymbol{k}) & g(\boldsymbol{k}) - is\lambda & i\lambda \\ g(\boldsymbol{k}) + is\lambda & \varepsilon_{yz}(\boldsymbol{k}) & -s\lambda \\ -i\lambda & -s\lambda & \varepsilon_{xy}(\boldsymbol{k}) \end{pmatrix}, \quad \text{(C2)}$$

where spin-orbit coupling is parametrized by λ, and the above energies are given by

$$\varepsilon_{xz}(\boldsymbol{k}) = -2t_1(1 - p)\cos k_x - 2t_2(1 + vp)\cos(k_y) - \mu, \quad \text{(C3)}$$

$$\varepsilon_{yz}(\boldsymbol{k}) = -2t_1(1 + vp)\cos k_y - 2t_2(1 - p)\cos(k_x) - \mu, \quad \text{(C4)}$$
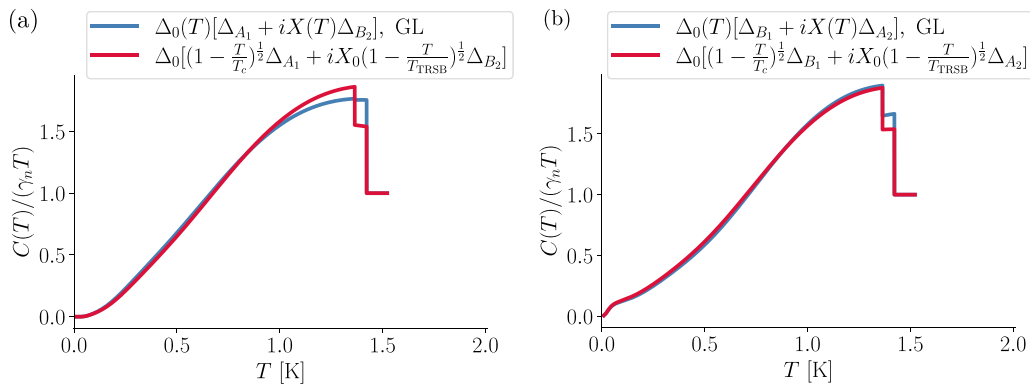

FIG. 13. Comparison of the heat capacity per temperature and normal-state value for the (a) $s' + id_{xy}$ and (b) $d_{x^2-y^2} + ig_{xy(x^2-y^2)}$ order parameters from Ref. [35] at zero strain using two different temperature dependencies. The blue lines show results using the Ginzburg-Landau solution, while the red lines use simple square root temperature dependencies and a constant $X_0 = 0.8$. In both cases it is seen that the nonanalyticity of $\Delta_0(T = T_{\text{TRSB}})$ reduces the second jump.
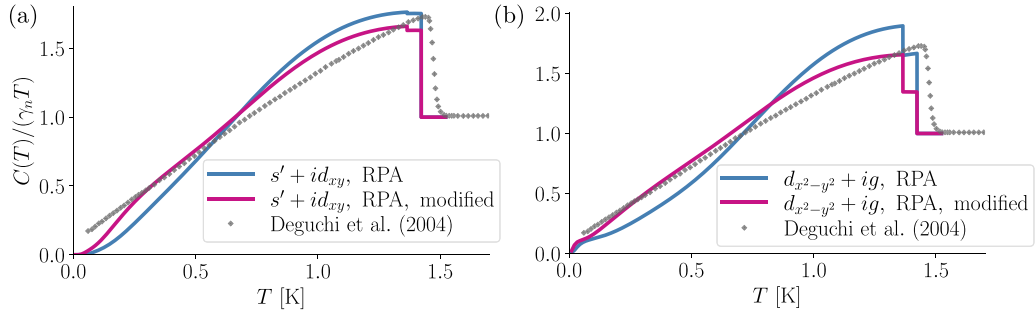
FIG. 14. Comparison of the heat capacity per temperature and normal-state value at zero strain using the Ginzburg-Landau solution with form factors obtained from microscopic RPA calculations [35] (blue lines) to a case where the band-resolved gap magnitudes have been redistributed to obtain a better fit (purple lines) with the experimental data of Ref. [63] (gray diamonds). Panel (a): The $s' + id_{xy}$ scenario. Here we redistributed $\Delta_\alpha/\Delta_\gamma = 0.7$ and $\Delta_\beta/\Delta_\gamma = 0.6$ as compared to the bare RPA form factors to obtain the purple line. Panel (b): The $d_{x^2-y^2} + ig_{xy(x^2-y^2)}$ scenario, where $\Delta_\alpha/\Delta_\gamma = 0.4$ and $\Delta_\beta/\Delta_\gamma = 0.5$ characterizes the purple line.

$$\begin{aligned}
\varepsilon_{xy}(\boldsymbol{k}) = &-2t_3[(1-p)\cos k_x + (1+\nu p)\cos k_y] \\
&- 4t_4 \cos k_x \cos k_y \\
&- 2t_5[(1-p)\cos(2k_x) + (1+\nu p)\cos(2k_y)] - \mu,
\end{aligned}$$
(C5)

$$g(\boldsymbol{k}) = -4t' \sin k_x \sin(k_y).$$
(C6)

Here (100) strain is parametrized by the deformation parameter p and the Poisson's ratio ν. The tight-binding parameters are summarized in Table II and are consistent with ARPES measurements [60].

APPENDIX D: ADDITIONAL RESULTS

In Figs. 11 and 12 we show supplementary plots of the order parameter components from Figs. 4 and 5 as a function of polar angle. In Fig. 13 we compare the heat capacity resulting from the Ginzburg-Landau theory, i.e., with an order parameter of the form

$$\Delta(T, \boldsymbol{p}) = \Delta_0(T)[f_a(\boldsymbol{p}) + iX(T)f_b(\boldsymbol{p})],$$
(D1)

with $X(T)$ and $\Delta_0(T)$ minimizing Eq. (8), to the results of using an order parameter of the form (cf. Ref. [36])

$$\Delta(T, \boldsymbol{p}) = \Delta_0\left[\sqrt{1 - \frac{T}{T_c}} f_a(\boldsymbol{p}) + iX_0\sqrt{1 - \frac{T}{T_{\text{TRSB}}}} f_b(\boldsymbol{p})\right],$$
(D2)

in both cases with the momentum-dependent components from Figs. 11 and 12 in the latter case with fixed $X_0 = 0.8$. In the case of both $s' + id_{xy}$ [panel (a)] and $d_{x^2-y^2} + ig_{xy(x^2-y^2)}$ [panel (b)] it is seen that the effect of the nonanalyticity of $\Delta_0(T)$ at $T = T_{\text{TRSB}}$ is a reduction of the second jump. In the case of panel (a) the second jump is almost vanishing for the Ginzburg-Landau solution.

TABLE II. Tight-binding parameters for Eqs. (C2) consistent with ARPES measurements [60], and Poisson's ratio ν applicable to (100) strain taken from Ref. [61].

Parameter	t_1	t_2	t_3	t_4	t_5	t'	μ	λ	ν
Value (meV)	88	9	80	40	5	4	109	45	0.508

In Fig. 14 we demonstrate that the match with the experimental heat capacity data of Ref. [63] can be somewhat improved by redistributing the band-resolved gap magnitudes compared to those obtained with the microscopic RPA calculations of Ref. [35]. A past study showed that by tuning interaction parameters of the theory it is possible to obtain a match with experimental data, albeit the study focused on an E_u (of D_{4h}) phase [89].

In Fig. 15 we provide supplementary results of the heat capacity for the same band structure, transition temperatures, and order parameter components as in Sec. III B, but for the reversed combination of orders, i.e., $d_{xy} + is'$ (strictly $B_1 + iA_1$ of D_2). The resulting second heat capacity jump is found to be $\eta = 0.260, 0.255, 0.356, 0.707, 1.496$ for $p = 0.0, -0.02, -0.03, -0.04, -0.05$, respectively. Not only does this rule out this specific $d_{xy} + is'$ order parameter as a viable candidate order for SRO [27], but it verifies the principles of Sec. II C. Physically, the B_1 component is nodal along $k_x, k_y = 0$, so if this component is the primary one, it leaves quasiparticles to be gapped out by the A_1 component (which is large at these points), resulting in a sizable second jump. This is qualitatively different from the case where the A_1 is the primary component. It should also be noted that the nodal regions of the B_1 component on the γ sheet grow with strain; see Fig. 4.
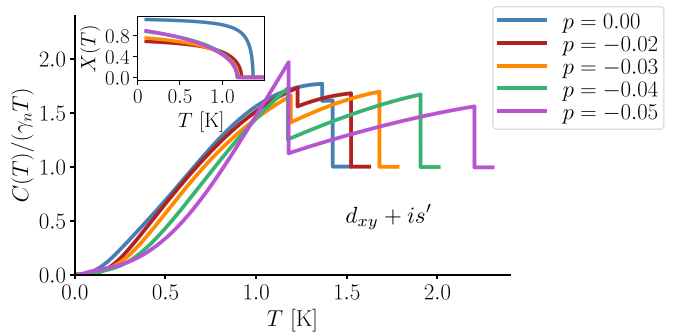

FIG. 15. Supplement to Fig. 7(a): Heat capacity for the $d_{xy} + is'$ order parameter. We used the order parameter ansatz of Eq. (1) with $\Delta_0(T)$ and $X(T)$ (inset) resulting from minimization of the free energy of Eq. (8), and with the momentum-dependent form factors of Fig. 4.
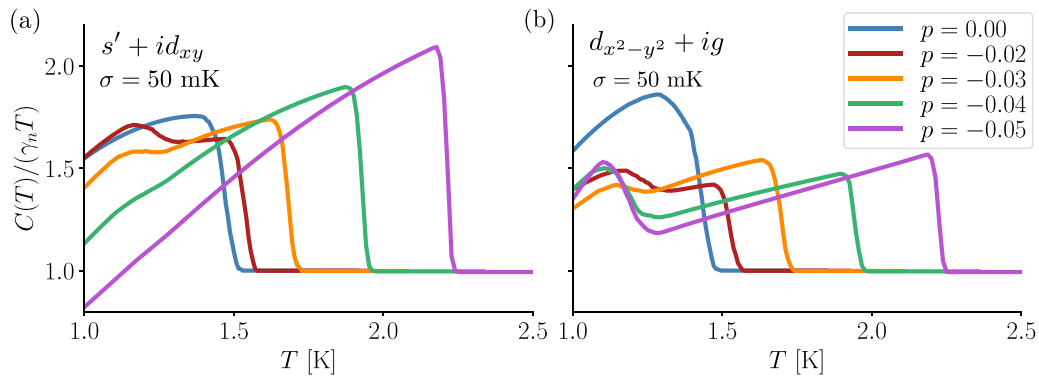
FIG. 16. Simulated effect of smearing with a transition width of $\sigma = 50$ mK in the (a) $s' + id_{xy}$ and (b) $d_{x^2-y^2} + ig_{xy(x^2-y^2)}$ order parameter scenario. See the caption of Fig. 8 for further details.

Finally, in Fig. 16 we supplement Fig. 8 with the simulated effect of a modest smearing of $\sigma = 50$ mK, which is in the lower end of the scale of the experimentally relevant transition widths [27]. In this case, the second jump is resolvable for both the $s' + id_{xy}$ and the $d_{x^2-y^2} + ig_{xy(x^2-y^2)}$ order parameters, at least for some strain values.

[1] S. K. Ghosh, M. Smidman, T. Shang, J. F. Annett, A. D. Hillier, J. Quintanilla, and H. Yuan, Recent progress on superconductors with time-reversal symmetry breaking, J. Phys.: Condens. Matter **33**, 033001 (2021).

[2] W.-C. Lee, S.-C. Zhang, and C. Wu, Pairing State with a Time-Reversal Symmetry Breaking in FeAs-Based Superconductors, Phys. Rev. Lett. **102**, 217002 (2009).

[3] C. N. Breiø, P. J. Hirschfeld, and B. M. Andersen, Supercurrents and spontaneous time-reversal symmetry breaking by nonmagnetic disorder in unconventional superconductors, Phys. Rev. B **105**, 014504 (2022).

[4] G. R. Stewart, Heavy-fermion systems, Rev. Mod. Phys. **56**, 755 (1984).

[5] R. Joynt and L. Taillefer, The superconducting phases of UPt$_3$, Rev. Mod. Phys. **74**, 235 (2002).

[6] S. Ran, C. Eckberg, Q.-P. Ding, Y. Furukawa, T. Metz, S. R. Saha, I.-L. Liu, M. Zic, H. Kim, J. Paglione, and N. P. Butch, Nearly ferromagnetic spin-triplet superconductivity, Science **365**, 684 (2019).

[7] D. Aoki, J.-P. Brison, J. Flouquet, K. Ishida, G. Knebel, Y. Tokunaga, and Y. Yanase, Unconventional superconductivity in UTe$_2$, J. Phys.: Condens. Matter **34**, 243002 (2022).

[8] W. Schlabitz, J. Baumann, B. Pollit, U. Rauchschwalbe, H. M. Mayer, U. Ahlheim, and C. D. Bredl, Superconductivity and magnetic order in a strongly interacting fermi-system: URu$_2$Si$_2$, Z. Phys. B **62**, 171 (1986).

[9] J. A. Mydosh and P. M. Oppeneer, Colloquium: Hidden order, superconductivity, and magnetism: The unsolved case of URu$_2$Si$_2$, Rev. Mod. Phys. **83**, 1301 (2011).

[10] Y. Maeno, H. Hashimoto, K. Yoshida, S. Nishizaki, T. Fujita, J. G. Bednorz, and F. Lichtenberg, Superconductivity in a layered perovskite without copper, Nature (London) **372**, 532 (1994).

[11] A. P. Mackenzie, T. Scaffidi, C. W. Hicks, and Y. Maeno, Even odder after twenty-three years: the superconducting order parameter puzzle of Sr$_2$RuO$_4$, npj Quantum Mater. **2**, 40 (2017).

[12] M. Rotter, M. Tegel, and D. Johrendt, Superconductivity at 38 K in the Iron Arsenide (Ba$_{1-x}$K$_x$)Fe$_2$As$_2$, Phys. Rev. Lett. **101**, 107006 (2008).

[13] J. Böker, P. A. Volkov, K. B. Efetov, and I. Eremin, $s + is$ superconductivity with incipient bands: Doping dependence and STM signatures, Phys. Rev. B **96**, 014517 (2017).

[14] A. D. Hillier, J. Quintanilla, and R. Cywinski, Evidence for Time-Reversal Symmetry Breaking in the Noncentrosymmetric Superconductor LaNiC$_2$, Phys. Rev. Lett. **102**, 117007 (2009).

[15] E. D. Bauer, N. A. Frederick, P.-C. Ho, V. S. Zapf, and M. B. Maple, Superconductivity and heavy fermion behavior in PrOs$_4$Sb$_{12}$, Phys. Rev. B **65**, 100506(R) (2002).

[16] Y. Aoki, A. Tsuchiya, T. Kanayama, S. R. Saha, H. Sugawara, H. Sato, W. Higemoto, A. Koda, K. Ohishi, K. Nishiyama, and R. Kadono, Time-Reversal Symmetry-Breaking Superconductivity in Heavy-Fermion PrOs$_4$Sb$_{12}$ Detected by Muon-Spin Relaxation, Phys. Rev. Lett. **91**, 067003 (2003).

[17] A. Pustogow, Y. Luo, A. Chronister, Y.-S. Su, D. A. Sokolov, F. Jerzembeck, A. P. Mackenzie, C. W. Hicks, N. Kikugawa, S. Raghu, S. E. Bauer, and E. D. Brown, Constraints on the superconducting order parameter in Sr$_2$RuO$_4$ from oxygen-17 nuclear magnetic resonance, Nature (London) **574**, 72 (2019).

[18] A. Chronister, A. Pustogow, N. Kikugawa, D. A. Sokolov, F. Jerzembeck, C. W. Hicks, A. P. Mackenzie, E. D. Bauer, and S. E. Brown, Evidence for even parity unconventional superconductivity in Sr$_2$RuO$_4$, Proc. Natl. Acad. Sci. USA **118**, e2025313118 (2021).

[19] T. Scaffidi, J. C. Romers, and S. H. Simon, Pairing symmetry and dominant band in Sr$_2$RuO$_4$, Phys. Rev. B **89**, 220510(R) (2014).

[20] H. S. Røising, T. Scaffidi, F. Flicker, G. F. Lange, and S. H. Simon, Superconducting order of Sr$_2$RuO$_4$ from a three-dimensional microscopic model, Phys. Rev. Res. **1**, 033108 (2019).

[21] A. T. Rømer, D. D. Scherer, I. M. Eremin, P. J. Hirschfeld, and B. M. Andersen, Knight Shift and Leading Superconducting Instability from Spin Fluctuations in Sr$_2$RuO$_4$, Phys. Rev. Lett. **123**, 247001 (2019).

[22] T. Scaffidi, Degeneracy between even- and odd-parity superconductivity in the quasi-1D Hubbard model and implications for Sr$_2$RuO$_4$, arXiv:2007.13769.

[23] X. Wang, Z. Wang, and C. Kallin, Higher angular momentum pairing states in Sr_2RuO_4 in the presence of longer-range interactions, Phys. Rev. B **106**, 134512 (2022).

[24] I. A. Firmo, S. Lederer, C. Lupien, A. P. Mackenzie, J. C. Davis, and S. A. Kivelson, Evidence from tunneling spectroscopy for a quasi-one-dimensional origin of superconductivity in Sr_2RuO_4, Phys. Rev. B **88**, 134521 (2013).

[25] R. Sharma, S. D. Edkins, Z. Wang, A. Kostin, C. Sow, Y. Maeno, A. P. Mackenzie, J. C. S. Davis, and V. Madhavan, Momentum-resolved superconducting energy gaps of Sr_2RuO_4 from quasiparticle interference imaging, Proc. Natl. Acad. Sci. USA **117**, 5222 (2020).

[26] S. NishiZaki, Y. Maeno, and Z. Mao, Changes in the superconducting state of Sr_2RuO_4 under magnetic fields probed by specific heat, J. Phys. Soc. Jpn. **69**, 572 (2000).

[27] Y.-S. Li, N. Kikugawa, D. A. Sokolov, F. Jerzembeck, A. S. Gibbs, Y. Maeno, C. W. Hicks, J. Schmalian, M. Nicklas, and A. P. Mackenzie, High-sensitivity heat-capacity measurements on Sr_2RuO_4 under uniaxial pressure, Proc. Natl. Acad. Sci. USA **118**, e2020492118 (2021).

[28] E. Hassinger, P. Bourgeois-Hope, H. Taniguchi, S. René de Cotret, G. Grissonnanche, M. S. Anwar, Y. Maeno, N. Doiron-Leyraud, and L. Taillefer, Vertical Line Nodes in the Superconducting Gap Structure of Sr_2RuO_4, Phys. Rev. X **7**, 011032 (2017).

[29] J. Xia, Y. Maeno, P. T. Beyersdorf, M. M. Fejer, and A. Kapitulnik, High Resolution Polar Kerr Effect Measurements of Sr_2RuO_4: Evidence for Broken Time-Reversal Symmetry in the Superconducting State, Phys. Rev. Lett. **97**, 167002 (2006).

[30] G. M. Luke, Y. Fudamoto, K. M. Kojima, M. I. Larkin, J. Merrin, B. Nachumi, Y. J. Uemura, Y. Maeno, Z. Q. Mao, Y. Mori, H. Nakamura, and M. Sigrist, Time-reversal symmetry-breaking superconductivity in Sr_2RuO_4, Nature (London) **394**, 558 (1998).

[31] S. Ghosh, A. Shekhter, F. Jerzembeck, N. Kikugawa, D. A. Sokolov, M. Brando, A. P. Mackenzie, C. W. Hicks, and B. J. Ramshaw, Thermodynamic evidence for a two-component superconducting order parameter in Sr_2RuO_4, Nat. Phys. **17**, 199 (2021).

[32] S. Benhabib, C. Lupien, I. Paul, L. Berges, M. Dion, M. Nardone, A. Zitouni, Z. Q. Mao, Y. Maeno, A. Georges, L. Taillefer, and C. Proust, Ultrasound evidence for a two-component superconducting order parameter in Sr_2RuO_4, Nat. Phys. **17**, 194 (2021).

[33] I. Žutić and I. Mazin, Phase-Sensitive Tests of the Pairing State Symmetry in Sr_2RuO_4, Phys. Rev. Lett. **95**, 217004 (2005).

[34] H. G. Suh, H. Menke, P. M. R. Brydon, C. Timm, A. Ramires, and D. F. Agterberg, Stabilizing even-parity chiral superconductivity in Sr_2RuO_4, Phys. Rev. Res. **2**, 032023(R) (2020).

[35] A. T. Rømer, P. J. Hirschfeld, and B. M. Andersen, Superconducting state of Sr_2RuO_4 in the presence of longer-range Coulomb interactions, Phys. Rev. B **104**, 064507 (2021).

[36] S. A. Kivelson, A. C. Yuan, B. J. Ramshaw, and R. Thomale, A proposal for reconciling diverse experiments on the superconducting state in Sr_2RuO_4, npj Quantum Mater. **5**, 43 (2020).

[37] R. Willa, M. Hecker, R. M. Fernandes, and J. Schmalian, Inhomogeneous time-reversal symmetry breaking in Sr_2RuO_4, Phys. Rev. B **104**, 024511 (2021).

[38] A. T. Rømer, T. A. Maier, A. Kreisel, P. J. Hirschfeld, and B. M. Andersen, Leading superconducting instabilities in three-dimensional models for Sr_2RuO_4, Phys. Rev. Res. **4**, 033011 (2022).

[39] G. Wagner, H. S. Røising, F. Flicker, and S. H. Simon, Microscopic Ginzburg-Landau theory and singlet ordering in Sr_2RuO_4, Phys. Rev. B **104**, 134506 (2021).

[40] M. Tinkham, *Introduction to Superconductivity* (McGraw-Hill, New York, 1975).

[41] L. P. Gor'kov, Microscopic derivation of the Ginzburg-Landau equations in the theory of superconductivity, Zh. Eksp. Teor. Fiz. **36**, 1918 (1959) [J. Exptl. Theoret. Phys. (U.S.S.R.) **9**, 1364 (1959)].

[42] S. M. Thomas, F. B. Santos, M. H. Christensen, T. Asaba, F. Ronning, J. D. Thompson, E. D. Bauer, R. M. Fernandes, G. Fabbris, and P. F. S. Rosa, Evidence for a pressure-induced antiferromagnetic quantum critical point in intermediate-valence UTe_2, Sci. Adv. **6**, eabc8709 (2020).

[43] B. Zinkl and M. Sigrist, Impurity-induced double transitions for accidentally degenerate unconventional pairing states, Phys. Rev. Res. **3**, L012004 (2021).

[44] K. M. Shen, N. Kikugawa, C. Bergemann, L. Balicas, F. Baumberger, W. Meevasana, N. J. C. Ingle, Y. Maeno, Z.-X. Shen, and A. P. Mackenzie, Evolution of the Fermi Surface and Quasiparticle Renormalization through a van Hove Singularity in $Sr_{2-y}La_yRuO_4$, Phys. Rev. Lett. **99**, 187001 (2007).

[45] V. Grinenko, D. Das, R. Gupta, B. Zinkl, N. Kikugawa, Y. Maeno, C. W. Hicks, H.-H. Klauss, M. Sigrist, and R. Khasanov, Unsplit superconducting and time reversal symmetry breaking transitions in Sr_2RuO_4 under hydrostatic pressure and disorder, Nat. Commun. **12**, 3920 (2021).

[46] J. E. Ortmann, J. Y. Liu, J. Hu, M. Zhu, J. Peng, M. Matsuda, X. Ke, and Z. Q. Mao, Competition between antiferromagnetism and ferromagnetism in Sr_2RuO_4 probed by Mn and Co doping, Sci. Rep. **3**, 2950 (2013).

[47] Y. Sheng, Y. Li, and Y.-f. Yang, Multipole-fluctuation pairing mechanism of $d_{x^2-y^2} + ig$ superconductivity in Sr_2RuO_4, Phys. Rev. B **106**, 054516 (2022).

[48] A. Steppke, L. Zhao, M. E. Barber, T. Scaffidi, F. Jerzembeck, H. Rosner, A. S. Gibbs, Y. Maeno, S. H. Simon, A. P. Mackenzie, and C. W. Hicks, Strong peak in T_c of Sr_2RuO_4 under uniaxial pressure, Science **355**, eaaf9398 (2017).

[49] F. Jerzembeck, H. S. Røising, A. Steppke, H. Rosner, D. A. Sokolov, N. Kikugawa, T. Scaffidi, S. H. Simon, A. P. Mackenzie, and C. W. Hicks, The superconductivity of Sr_2RuO_4 under c-axis uniaxial stress, Nat. Commun. **13**, 4596 (2022).

[50] A. T. Rømer, A. Kreisel, I. Eremin, M. A. Malakhov, T. A. Maier, P. J. Hirschfeld, and B. M. Andersen, Pairing symmetry of the one-band Hubbard model in the paramagnetic weak-coupling limit: A numerical RPA study, Phys. Rev. B **92**, 104505 (2015).

[51] V. Grinenko, S. Ghosh, R. Sarkar, J.-C. Orain, A. Nikitin, M. Elender, D. Das, Z. Guguchia, F. Brückner, M. E. Barber, J. Park, N. Kikugawa, D. A. Sokolov, J. S. Bobowski, T. Miyoshi, Y. Maeno, A. P. Mackenzie, H. Luetkens, C. W. Hicks, and H.-H. Klauss, Split superconducting and time-reversal symmetry-breaking transitions in Sr_2RuO_4 under stress, Nat. Phys. **17**, 748 (2021).

[52] C. W. Hicks, J. R. Kirtley, T. M. Lippman, N. C. Koshnick, M. E. Huber, Y. Maeno, W. M. Yuhasz, M. B. Maple, and K. A. Moler, Limits on superconductivity-related magnetization

in Sr_2RuO_4 and $PrOs_4Sb_{12}$ from scanning SQUID microscopy, Phys. Rev. B **81**, 214501 (2010).

[53] S. Bhattacharyya, A. Kreisel, X. Kong, T. Berlijn, A. T. Rømer, B. M. Andersen, and P. J. Hirschfeld, Superconducting gap symmetry from Bogoliubov quasiparticle interference analysis on Sr_2RuO_4, arXiv:2109.10712.

[54] K. D. Nelson, Z. Q. Mao, Y. Maeno, and Y. Liu, Odd-parity superconductivity in Sr_2RuO_4, Science **306**, 1151 (2004).

[55] F. Kidwingira, J. D. Strand, D. J. V. Harlingen, and Y. Maeno, Dynamical superconducting order parameter domains in Sr_2RuO_4, Science **314**, 1267 (2006).

[56] M. S. Anwar, M. Kunieda, R. Ishiguro, S. R. Lee, L. A. B. Olde Olthof, J. W. A. Robinson, S. Yonezawa, T. W. Noh, and Y. Maeno, Observation of superconducting gap spectra of long-range proximity effect in $Au/SrTiO_3/SrRuO_3/Sr_2RuO_4$ tunnel junctions, Phys. Rev. B **100**, 024516 (2019).

[57] J. Jang, D. G. Ferguson, V. Vakaryuk, R. Budakian, S. B. Chung, P. M. Goldbart, and Y. Maeno, Observation of half-height magnetization steps in Sr_2RuO_4, Science **331**, 186 (2011).

[58] A. C. Yuan, E. Berg, and S. A. Kivelson, Strain-induced time reversal breaking and half quantum vortices near a putative superconducting tetracritical point in Sr_2RuO_4, Phys. Rev. B **104**, 054518 (2021).

[59] S. Kittaka, S. Nakamura, T. Sakakibara, N. Kikugawa, T. Terashima, S. Uji, D. A. Sokolov, A. P. Mackenzie, K. Irie, Y. Tsutsumi, K. Suzuki, and K. Machida, Searching for gap zeros in Sr_2RuO_4 via field-angle-dependent specific-heat measurement, J. Phys. Soc. Jpn. **87**, 093703 (2018).

[60] V. Zabolotnyy, D. Evtushinsky, A. Kordyuk, T. Kim, E. Carleschi, B. Doyle, R. Fittipaldi, M. Cuoco, A. Vecchione, and S. Borisenko, Renormalized band structure of Sr_2RuO_4: A quasiparticle tight-binding approach, J. Electron. Spectrosc. Relat. Phenom. **191**, 48 (2013).

[61] M. E. Barber, F. Lechermann, S. V. Streltsov, S. L. Skornyakov, S. Ghosh, B. J. Ramshaw, N. Kikugawa, D. A. Sokolov, A. P. Mackenzie, C. W. Hicks, and I. I. Mazin, Role of correlations in determining the Van Hove strain in Sr_2RuO_4, Phys. Rev. B **100**, 245139 (2019).

[62] A. T. Rømer, A. Kreisel, M. A. Müller, P. J. Hirschfeld, I. M. Eremin, and B. M. Andersen, Theory of strain-induced magnetic order and splitting of T_c and T_{TRSB} in Sr_2RuO_4, Phys. Rev. B **102**, 054506 (2020).

[63] K. Deguchi, Z. Q. Mao, and Y. Maeno, Determination of the superconducting gap structure in all bands of the spin-triplet superconductor Sr_2RuO_4, J. Phys. Soc. Jpn. **73**, 1313 (2004).

[64] Experimentally, the size of the gap has been inferred from STM measurements to be about 350 μeV [25].

[65] B. M. Andersen, P. J. Hirschfeld, A. P. Kampf, and M. Schmid, Disorder-Induced Static Antiferromagnetism in Cuprate Superconductors, Phys. Rev. Lett. **99**, 147002 (2007).

[66] M. N. Gastiasoro, F. Bernardini, and B. M. Andersen, Unconventional Disorder Effects in Correlated Superconductors, Phys. Rev. Lett. **117**, 257002 (2016).

[67] G. Bruls, D. Weber, B. Wolf, P. Thalmeier, B. Lüthi, A. de Visser, and A. Menovsky, Strain–order-parameter coupling and phase diagrams in superconducting UPt_3, Phys. Rev. Lett. **65**, 2294 (1990).

[68] E. R. Schemm, W. J. Gannon, C. M. Wishne, W. P. Halperin, and A. Kapitulnik, Observation of broken time-reversal symmetry in the heavy-fermion superconductor UPt_3, Science **345**, 190 (2014).

[69] G. M. Luke, A. Keren, L. P. Le, W. D. Wu, Y. J. Uemura, D. A. Bonn, L. Taillefer, and J. D. Garrett, Muon spin relaxation in UPt_3, Phys. Rev. Lett. **71**, 1466 (1993).

[70] P. D. de Réotier, A. Huxley, A. Yaouanc, J. Flouquet, P. Bonville, P. Imbert, P. Pari, P. Gubbens, and A. Mulders, Absence of zero field muon spin relaxation induced by superconductivity in the B phase of UPt_3, Phys. Lett. A **205**, 239 (1995).

[71] C. Kallin and J. Berlinsky, Chiral superconductors, Rep. Prog. Phys. **79**, 054502 (2016).

[72] R. A. Fisher, S. Kim, B. F. Woodfield, N. E. Phillips, L. Taillefer, K. Hasselbach, J. Flouquet, A. L. Giorgi, and J. L. Smith, Specific heat of UPt_3: Evidence for unconventional superconductivity, Phys. Rev. Lett. **62**, 1411 (1989).

[73] G. J. McMullan, P. M. C. Rourke, M. R. Norman, A. D. Huxley, N. Doiron-Leyraud, J. Flouquet, G. G. Lonzarich, A. McCollam, and S. R. Julian, The Fermi surface and f-valence electron count of UPt_3, New J. Phys. **10**, 053029 (2008).

[74] T. Trappmann, H. v. Löhneysen, and L. Taillefer, Pressure dependence of the superconducting phases in UPt_3, Phys. Rev. B **43**, 13714(R) (1991).

[75] I. M. Hayes, D. S. Wei, T. Metz, J. Zhang, Y. S. Eo, S. Ran, S. R. Saha, J. Collini, N. P. Butch, D. F. Agterberg, A. Kapitulnik, and J. Paglione, Multicomponent superconducting order parameter in UTe_2, Science **373**, 797 (2021).

[76] D. Braithwaite, M. Vališka, G. Knebel, G. Lapertot, J.-P. Brison, A. Pourret, M. E. Zhitomirsky, J. Flouquet, F. Honda, and D. Aoki, Multiple superconducting phases in a nearly ferromagnetic system, Commun. Phys. **2**, 147 (2019).

[77] C. Girod, C. R. Stevens, A. Huxley, E. D. Bauer, F. B. Santos, J. D. Thompson, R. M. Fernandes, J.-X. Zhu, F. Ronning, P. F. S. Rosa, and S. M. Thomas, Thermodynamic and electrical transport properties of UTe_2 under uniaxial stress, Phys. Rev. B **106**, L121101 (2022).

[78] P. F. S. Rosa, A. Weiland, S. S. Fender, B. L. Scott, F. Ronning, J. D. Thompson, E. D. Bauer, and S. M. Thomas, Single thermodynamic transition at 2 K in superconducting UTe_2 single crystals, Commun. Mater. **3**, 33 (2022).

[79] K. Machida, Theory of spin-polarized superconductors — An analogue of superfluid ^3He A-phase—, J. Phys. Soc. Jpn. **89**, 033702 (2020).

[80] L. Jiao, S. Howard, S. Ran, Z. Wang, J. O. Rodriguez, M. Sigrist, Z. Wang, N. P. Butch, and V. Madhavan, Chiral superconductivity in heavy-fermion metal UTe_2, Nature (London) **579**, 523 (2020).

[81] H. R. Ott, H. Rudigier, Z. Fisk, and J. L. Smith, Phase transition in the superconducting state of $U_{1-x}Th_xBe_{13}$ ($x = 0-0.06$), Phys. Rev. B **31**, 1651 (1985).

[82] R. H. Heffner, J. L. Smith, J. O. Willis, P. Birrer, C. Baines, F. N. Gygax, B. Hitti, E. Lippelt, H. R. Ott, A. Schenck, E. A. Knetsch, J. A. Mydosh, and D. E. MacLaughlin, New Phase Diagram for $(U,Th)Be_{13}$: A Muon-Spin-Resonance and H_{c1} Study, Phys. Rev. Lett. **65**, 2816 (1990).

[83] Y. Shimizu, S. Kittaka, S. Nakamura, T. Sakakibara, D. Aoki, Y. Homma, A. Nakamura, and K. Machida, Quasiparticle excitations and evidence for superconducting double transitions in monocrystalline $U_{0.97}Th_{0.03}Be_{13}$, Phys. Rev. B **96**, 100505(R) (2017).

[84] J. Goryo, Phenomenology for multiple phases in the heavy-fermion skutterudite superconductor PrOs$_4$Sb$_{12}$, Phys. Rev. B **67**, 184511 (2003).

[85] L. Shu, W. Higemoto, Y. Aoki, A. D. Hillier, K. Ohishi, K. Ishida, R. Kadono, A. Koda, O. O. Bernal, D. E. MacLaughlin, Y. Tunashima, Y. Yonezawa, S. Sanada, D. Kikuchi, H. Sato, H. Sugawara, T. U. Ito, and M. B. Maple, Suppression of time–reversal symmetry breaking superconductivity in Pr(Os$_{1-x}$Ru$_x$)$_4$Sb$_{12}$ and Pr$_{1-y}$La$_y$Os$_4$Sb$_{12}$, Phys. Rev. B **83**, 100504(R) (2011).

[86] M. B. Maple, P.-C. Ho, N. A. Frederick, V. S. Zapf, W. M. Yuhasz, E. D. Bauer, A. D. Christianson, and A. H. Lacerda, Superconductivity and the high-field ordered phase in the heavy-fermion compound PrOs$_4$Sb$_{12}$, J. Phys.: Condens. Matter **15**, S2071 (2003).

[87] M.-A. Measson, D. Braithwaite, J. Flouquet, G. Seyfarth, J. P. Brison, E. Lhotel, C. Paulsen, H. Sugawara, and H. Sato, Superconducting phase diagram of the filled skuterrudite PrOs$_4$Sb$_{12}$, Phys. Rev. B **70**, 064516 (2004).

[88] A. A. Abrikosov, L. P. Gor'kov, and I. E. Dzyaloshinskii, On the application of quantum-field-theory methods to problems of quantum statistics at finite temperatures, Zh. Eksp. Teor. Fiz. **36**, 900 (1959) [J. Exptl. Theoret. Phys. (U.S.S.R) **9**, 636 (1959)].

[89] T. Nomura and K. Yamada, Detailed investigation of gap structure and specific heat in the *p*-wave superconductor Sr$_2$RuO$_4$, J. Phys. Soc. Jpn. **71**, 404 (2002).